Chapter 1.   Introduction

1-1.   Photonic Crystals

The concept of photonic crystals was first proposed by Prof. Yablonovitch in 1987 [1]. In recent years, this concept and its applications have attracted a lot of attentions. The periodic index variation in dielectric materials is one of the significant characteristics of photonic crystals. Photonic crystals can be divided into three categories which are periodic in one, two, and three directions as shown in Fig. 1-1 [2]. One-dimensional and two-dimensional photonic crystals are widely used in real applications due to easier fabrication than that of three-dimensional photonic crystals. In my thesis, I will focus on two-dimensional photonic crystals.
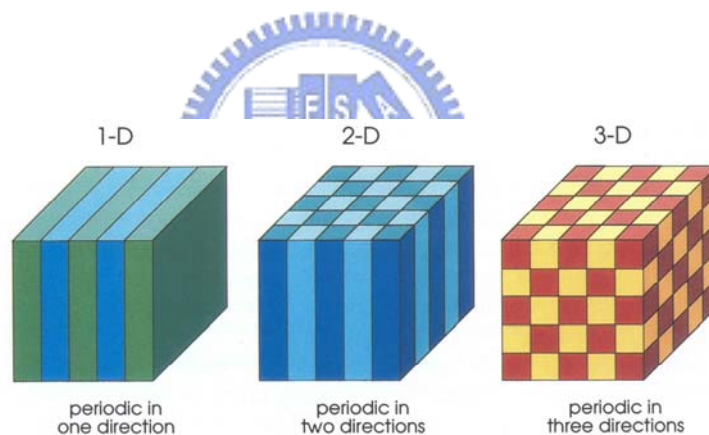

Fig. 1-1.   Photonic crystals can be divided into one-, two-, and three-dimensional photonic crystals. (Adopted from reference [2].)

Another important characteristic of photonic crystals is the photonic band-gap. If we design the photonic crystals properly, the light will be prevented from propagating in certain directions with specific frequencies. A well-known example is distributed Bragg reflectors (DBRs). The basic structure of DBRs is a steak of two dielectric materials with different refractive indices as shown in Fig. 1-2 [3]. In fact, it is a typical one-dimensional photonic crystal structure. As we can see in Fig. 1-2, the reflectivity of this structure between the light

wavelengths 800 nm to 1200 nm is equal to one. The light in this wavelength range will be

suffered from total internal reflection (TIR), i.e. its propagating will be "forbidden" in this

structure. This TIR wavelength range is so-called "photonic band-gap".
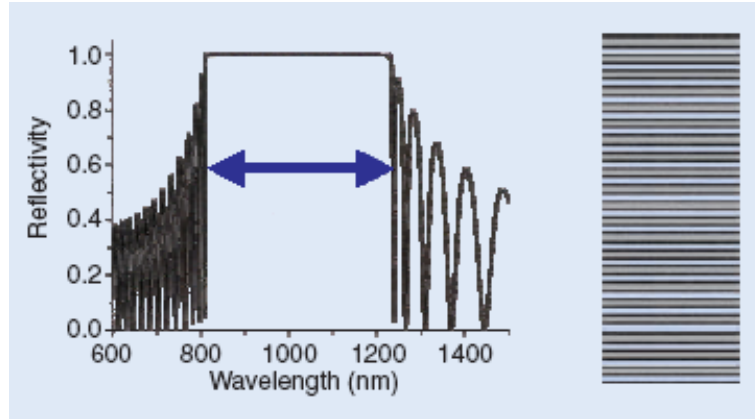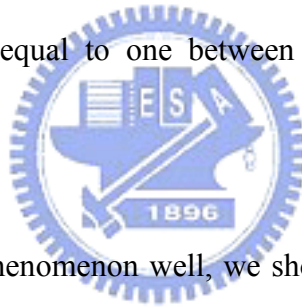

Fig. 1-2. The reflection spectrum and the structure of distributed Bragg reflectors (DBRs).
The reflectivity is equal to one between 800nm and 1200nm. (Adopted from
reference [3].)

In order to explain this phenomenon well, we should take a look at the well-developed

electronic material theory first. In the crystal structures, atoms or molecules are arranged

periodic in space. The behaviors of electrons will be affected by this periodic arrangement.

The behaviors can be illustrated by time-independent Shordinger equation:

$$[-\frac{\hbar^2}{2m}+V(r)]\Psi(r)=E\Psi(r) \tag{1}$$

In this equation, the V(r) term can be approximated to be a periodic potential function due to

the periodic arrangement of atoms or molecules in the crystal. The square of Ψ(r) denotes the

existence probabilities of electrons in space. In some cases, there would be destructive

interferences of electrons with certain energies due to Bragg-like diffraction. When this

happens, the Ψ(r) term is equal to zero, i.e. there are no electrons exist in some energy levels.

This is the well-known electronic band-gap. In addition, if the potential function is strong

enough, the gap might extend to all directions, resulting in a "complete band-gap".

The phenomenon of photonic band-gap can be regarded as the optical analogy of electronic material systems. The periodic refractive index variation provides the periodic potential function instead of atoms in crystal. Photons in photonic crystals will be affected by this function. This can produce phenomena for photons as the atomic potential function does for electrons, i.e. light with specific energies in certain directions will be prevented from propagating in the dielectric materials.

The behavior of photons in photonic crystals can be illustrated by the following master equation:

$$\nabla \times (\frac{1}{\varepsilon(r)} \nabla \times H(r)) = (\frac{w}{c})^2 H(r) \qquad (2)$$

For a given ε(r) which denotes the dielectric constant variation function in space, one can solve the master equation to find the modes H(r) for a given frequency. As a result, the eigen-values and the corresponding eigen-vectors can be obtained. Also we can obtain the band diagrams of photonic crystals.

For example, we calculate the band diagram of two-dimensional photonic crystals with 500nm lattice constant and 140nm hole radius by using two-dimensional plane-wave-expansion (PWE) method as shown in Fig. 1-3. The index of the material is 3.4. In this figure, the x-axis and y-axis denote the wave vector and the normalized frequency a/λ. As one can see there are no eigen-values in the shadow region, i.e. light propagating in this frequency range is forbidden in the dielectric material. This shadow region is so-called "photonic band-gap".
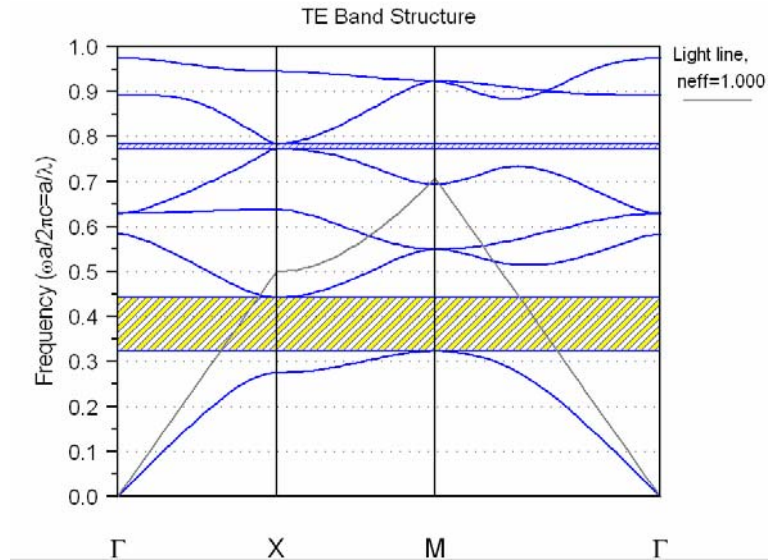
Fig. 1-3.   This is a typical TE band diagram of two-dimensional photonic crystal. There is a band gap between the first band and the second band. In this case, "TE" denotes light with electric field in the plane of the crystal.

The abilities to control light become possible because of the photonic band-gap. One could construct the defects by removing parts of the periodic structure in photonic crystals. As shown in Fig. 1-4(a) and (b), a line defect and a point defect are formed by removing a row of air holes and a single air hole in two-dimensional photonic crystal slabs. In these defects, light in specific frequencies can propagate with very low loss. A lot of excellent ideas have been demonstrated and reported in recent years, such as photonic crystal waveguides, micro-cavities, emitters, super-lens, and so on. In my thesis, I will focus on the photonic crystal micro-cavity lasers.
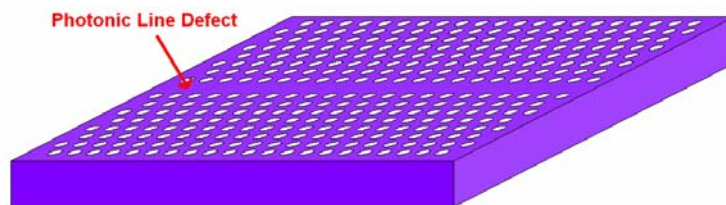

(a)
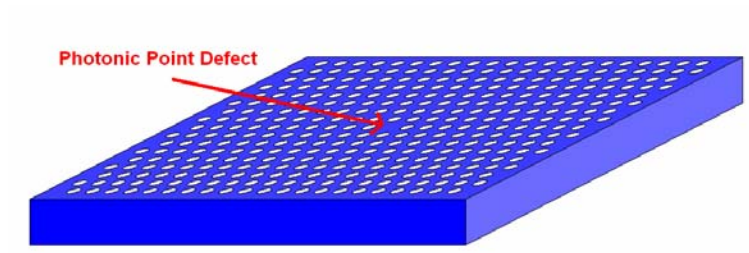
(b)

Fig. 1-4. (a). A photonic crystal line defect is formed by removing one or more rows of the air holes. This kind of defect has been widely used in low-loss photonic crystal waveguides. (b). A photonic crystal point defect is formed by single or more missing air holes. This is widely used to construct the photonic crystal micro-cavities and nano-cavities.

1-2. Two-Dimensional Photonic Crystal Lasers

Purcell predicted that spontaneous emission can be altered by modification of the optical radiation field in 1946 [4], and one could achieve this by placing a gain medium in a cavity structure. This cavity can be formed by surrounding mirrors using facet and DBRs. Although there have been high performance vertical-cavity surface-emitting lasers (VCSELs) and micro-disk lasers in real applications, some characteristics can not be achieved such as ultra-low threshold, high quality factor, and small mode volume when the device sizes are minimized. This is caused by the optical loss in small dimensions of these devices.

Since the photonic crystal concept was proposed, the photonic band-gap could be used to accomplish above advantages. A semiconductor laser with high quality factor, small mode volume, and ultra-low threshold could be possible because of the low loss property due to the photonic band-gap. This kind of device can be potential light source in optical communication systems, especially in WDM systems.
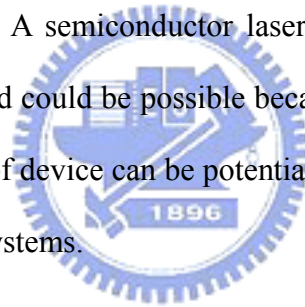
The typical configuration of a two-dimensional photonic crystal laser is shown in Fig. 1-5 [5]. In Fig. 1-5, the photonic crystal patterns are defined on the two-dimensional dielectric slab which consists of several quantum wells or quantum dots. And a micro-cavity is formed by several missing air holes in photonic crystal patterns. The undercut is fabricated in order to form a symmetric waveguide structure. In this structure, the vertical confinement is provided by a symmetric waveguide structure and the photonic crystal pattern provides the in-plane confinement by its well-known photonic band-gap.
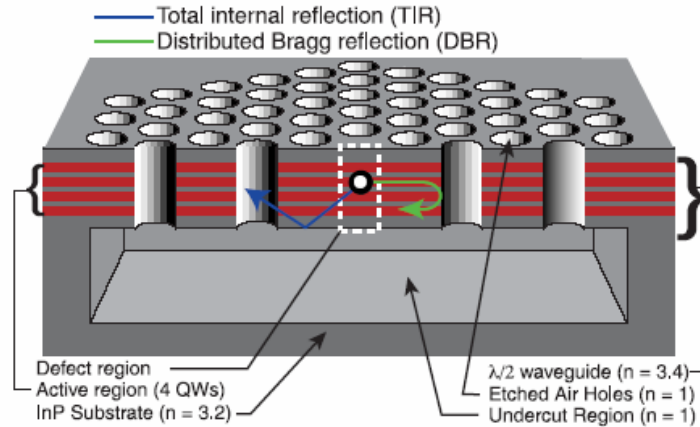
Fig. 1-5.　The basic structure of two-dimensional photonic crystals laser. (Adopted from reference [5].)

The basic photonic crystal micro-cavity lasers with triangular lattice [6, 7] and square lattice [8, 9] have been widely investigated. The triangular lattice photonic crystal lasers are much easier to demonstrate than the square lattice photonic crystal lasers because of the larger band-gap. This can be easily proved by three-dimensional plane-wave expansion (PWE) method as shown in Fig. 1-6.(a) and (b). The simulation conditions are both 0.26 r/a ratio with 500nm lattice constant. However, the square lattice photonic crystal lasers could be a good candidate of low-threshold photonic crystal lasers with small mode volume due to its lowest whisper-gallery-mode [10]. In the following chapters, I will focus on two-dimensional photonic crystal lasers with triangular lattice.
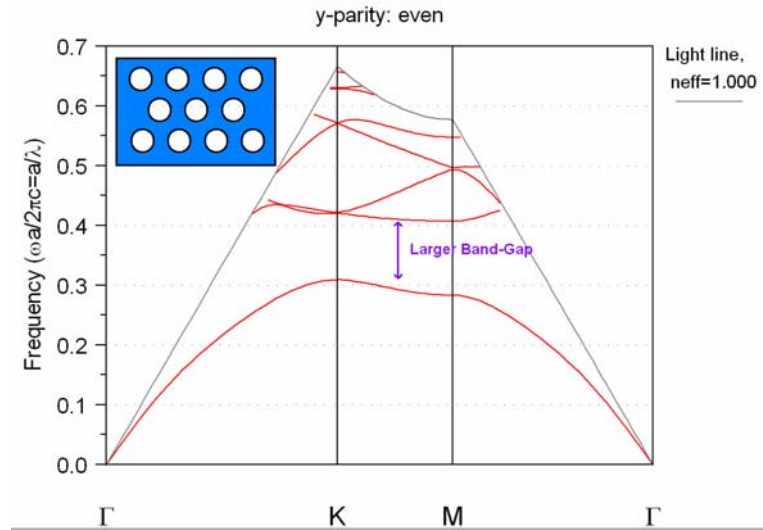
(a)
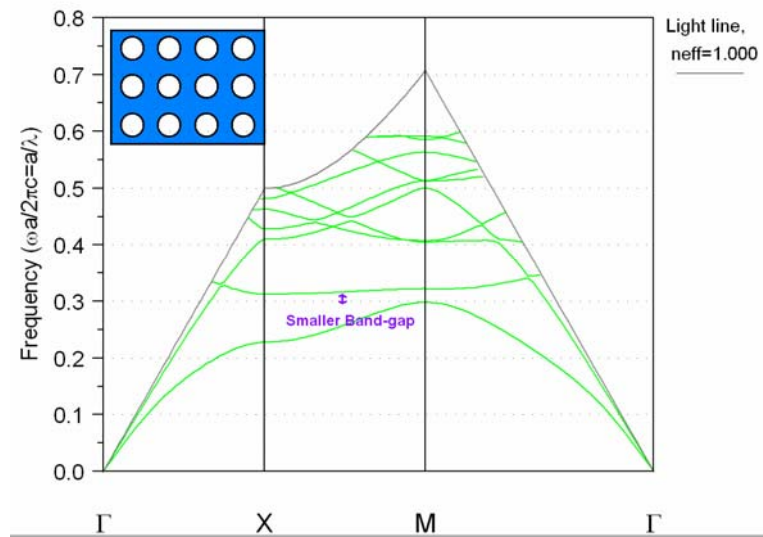
(b)

Fig. 1-6. The typical TE-like band diagrams of two-dimensional photonic crystal slabs with (a) triangular lattice and (b) square lattice. The band-gap of triangular lattice is much larger than that of square lattice with the same r/a ratio.

1-3. History and Developments

The concept of photonic crystal lasers was first proposed in 1994 [11]. In 1999, two-dimensional photonic crystal lasers were first demonstrated by O. Painter et al. at Caltech [5]. As we mentioned before, they are potential light sources in optical communication systems due to several advantages. More and more photonic crystal defect lasers were reported in recent years. All of these can be divided into photonic-cavity lasers and band-edge emitting lasers. In this section, I will introduce the history and developments of photonic crystal micro-cavity lasers in recent years briefly.

Most researchers focused on different characteristics of 2D photonic crystal lasers such as ultra-low threshold, high quality (Q) factor, high side mode suppression ratio, high β value, and small mode volume.

In order to obtain the improved characteristics of photonic crystal lasers, more and more researchers focus on the modification of photonic crystal patterns and the micro-cavity geometry. The photonic crystal lasers with ultra-low threshold, high Q factor, and high β value can be achieved by different modification of photonic crystal patterns including mismatching of the surrounding photonic crystal and shrinking of the air-holes near the micro-cavities [12-14]. A lot of excellent ideas have been reported in these years.

In addition, there is a trade-off between minimizing the device size and the quality factor. Although the single defect photonic crystal lasers have the advantage of operating in a single mode with a very small mode volume, the larger cavity size would still be an important application due to the high quality factor caused by the larger photon lifetime.

At last, most of these photonic crystal lasers reported in recent years are under pulsed operation due to lack of heat sink. This is caused by the low thermal conductivity of the air claddings in the generally-used membrane structure, i.e. high index-contrast structure. This could be a big problem for the improvement towards continuous-wave operation and electrical injection for this device in the future. Although there have been reports about continuous-wave operation of photonic crystal lasers, the sizes of these cavities are still quite large [15, 16].

In addition, the serious surface recombination of photonic crystals, doping, and contact loss should be solved to achieve the electrical injection of photonic crystal lasers. In 2004, the first electrical-driven single defect photonic crystal micro-cavity lasers with ultra-high β value and the lower threshold than the general VCSELs were demonstrated by H.-G. Park et al [17]. The simple illustration of this device is shown in Fig. 1-7 (a) and the L-I curve is shown in Fig. 1-7 (b) [17]. This is a great improvement in photonic crystal micro-cavity laser technologies. And it is believed that there will be more and more excellent achievements in the future.
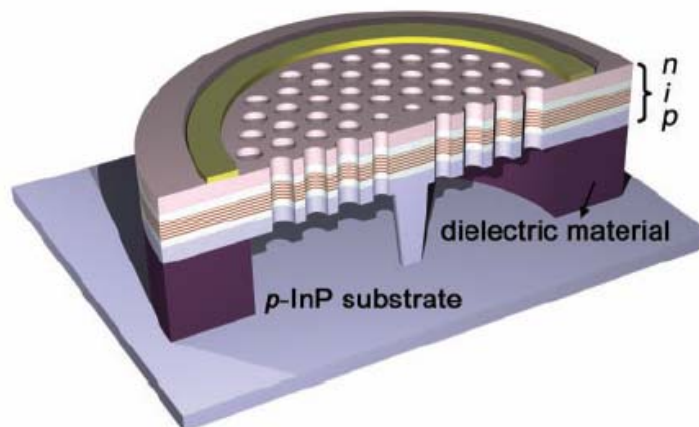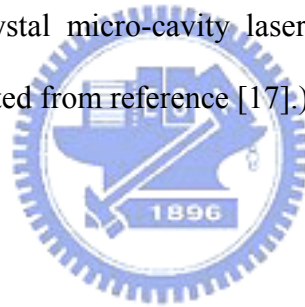

(a)
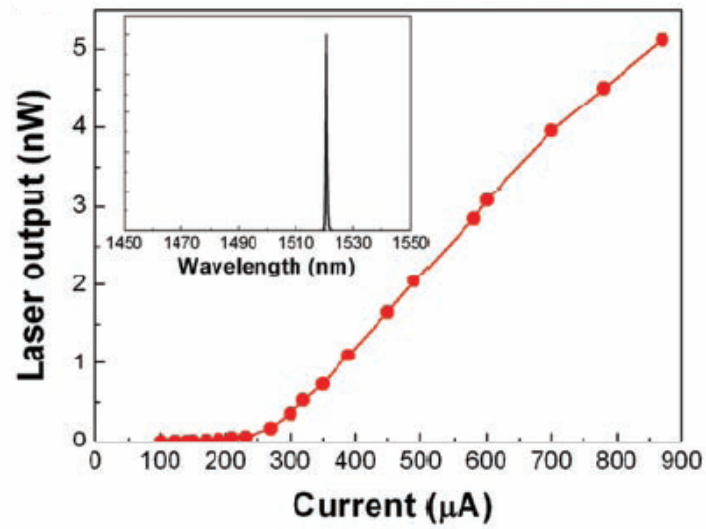
(b)

Fig. 1-7. (a) The illustration of the structure with central post for electrically-driven single defect photonic crystal micro-cavity laser. (b) The L-I curve of this photonic crystal laser. (Adopted from reference [17].)

1-4. Motivation and Overview of Thesis

Two-dimensional photonic crystal laser is a very attractive device for optical communication system. In order to achieve the properties of high Q factor, low threshold, and small mode volume of photonic crystal micro-cavity, the basic fabrication, simulation tools, and measurement system have to be setup.

In this thesis, the simulation, fabrication, and characterization of two-dimensional photonic crystal lasers are investigated. In chapter 2, the band diagrams and defect modes of two-dimensional photonic crystal micro-cavity are calculated in order to design and optimize the devices. In chapter 3, the fabrications of two different structures of two-dimensional photonic crystal lasers are introduced. In chapter 4, the basic lasing characteristics of two-dimensional photonic crystal laser are measured by a NIR micro-photo-luminescence (PL) system. The tuning properties of lasing wavelength are also investigated. We also measure and discuss the thermal properties of two-dimensional photonic crystal membrane laser by a thermo-electro cooler (TEC) system.

2. Structure Design

In order to design two-dimensional photonic crystal lasers, the band diagrams and defect modes of different photonic crystal parameters should be calculated. In this chapter, they are calculated by 3D PWE method and two-dimensional finite-difference time-domain (FDTD) method.

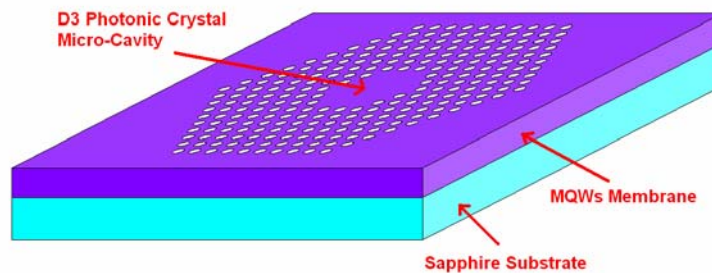## 2-1. Band Diagrams of Membrane Structures and Asymmetric Structures

2-1-1. Membrane Structure and Asymmetric Structure

There are two different structures of two-dimensional photonic crystal lasers. One is membrane structure, and the other is asymmetric structure. The illustrations of the two structures are shown in Fig. 2-1 (a) and (b). The membrane structure is formed by multi-quantum-wells (MQWs) membrane surrounded by air-claddings. The effective index of the InP-based material is about 3.4. This material is a good candidate in fabricating photonic crystal lasers because of it relative low surface recombination rate.

In asymmetric structure, the dielectric photonic crystal slab is still the same but one side of air-claddings is replaced by a sapphire substrate with a refractive index 1.6. There are two reasons of choosing sapphire as our new substrate. First, the thermal conductivity of sapphire is over 2000 times higher than that of air. This could help us to solve thermal problems in the membrane structure. Second, sapphire is a relative low index material which can still provide sufficient vertical confinement. But compared to membrane structure, there is larger optical loss in substrate side and this will lead to lower Q factor of the defect modes. The fabrication and more discussions of these two structures will be presented in the following chapters.
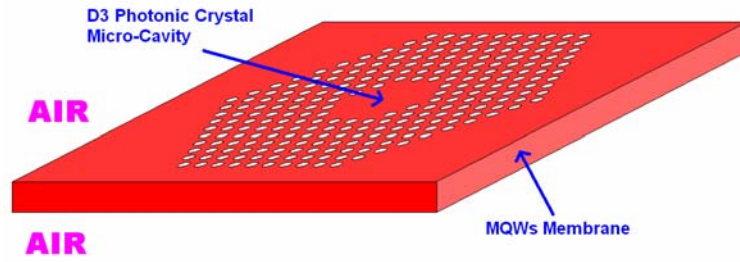
(a)

(b)

Fig. 2-1.   The illustrations of two-dimensional photonic crystal (a) membrane structure and

(b) asymmetric structure. The "D3" means that the micro-cavity is formed by

three-period missing air holes, i.e. 19 missing air holes.

2-1-2. Band Diagrams

At first, some important parameters and their definitions in the following simulations are

listed in Table 2-1.

The photonic crystal pattern of membrane structure is defined on a 220nm dielectric slab

which only supports the TE fundamental mode. The index profile of the two-dimensional

photonic crystal membrane structure is shown in Fig. 2-2. A typical band diagram of TE-like

bands with 500nm lattice constant and 0.3 r/a ratio, i.e. 150nm air hole radius, is shown in Fig.

2-3. In this band diagram, the first band is so-called "dielectric band" with the lower

normalized frequency and the second band is so-called "air band" with the higher normalized frequency. There is a forbidden band between the first two bands over all wave vectors below the light line which denotes the interface between the dielectric slab and the air-claddings.

Table. 2-1.   Important parameters of two-dimensional photonic crystal slabs.

Symbol	Denote	Definition
a	Lattice Constant	The distance of the two neighboring air-holes.
r	Air Hole Radius	The radius of the air-holes.
d	Slab Thickness	The thickness of the two-dimensional slab that photonic crystal patterns defined on.
n_{slab}	Index of the slab	Index of the slab
n_{hole}	Index of the hole	Index of the hole

In order to optimize the alignment between the photon-luminescence (PL) spectrum of the MQWs and the photonic band-gap, the band diagrams with different r/a ratio are calculated. The variation of the band-gap with different r/a ratio is shown in Fig. 2-4. In this simulation, the lattice constant and the membrane thickness are fixed at 500nm and 220nm. The photonic bands will shift to the higher normalized frequencies when low dielectric material components increases, i.e. r/a ratio increases, and vice versa. In Fig. 2-4, the band-gap also increases with increasing r/a ratio.
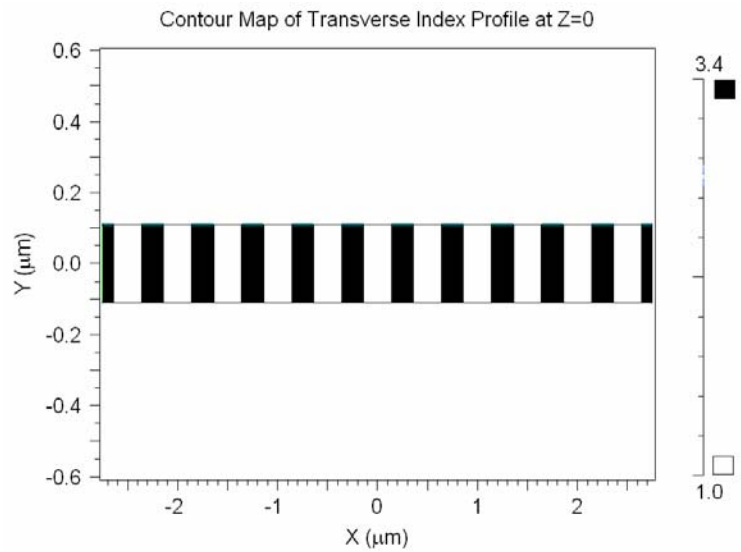
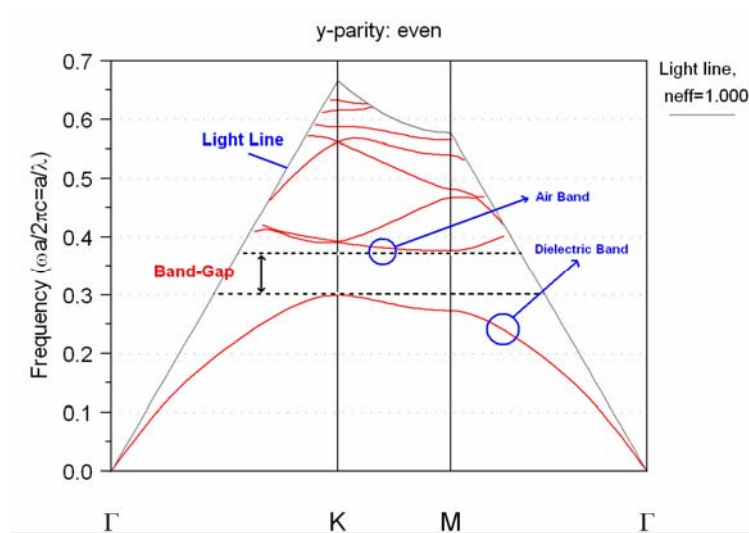Fig. 2-2.   The index profile of a two-dimensional photonic crystal membrane structure.

Fig. 2-3.   The TE-like band diagram of a two-dimensional photonic crystal membrane with 0.3 r/a ratio and 500 nm lattice constant. In three-dimensional simulation, the modes are classified as even (TE-like) modes or odd (TM-like) modes.

The thickness of the dielectric slab also affects the band diagram. The variation of the band-gap caused by this factor is shown in Fig. 2-5. It is easy to understand that the effective index of the slab increases when the thickness increases. The band diagram will shift to lower normalized frequency when the effective index increases. However, we do not change its

thickness because of the availability of InGaAsP/InP MQWs wafers. According to the simulation and our target wavelength 1550nm, the thickness between 200nm and 260nm should be chosen because of the band-gap position and the reason of supporting the TE fundamental mode. In this simulation, the r/a ratio is fixed at 0.26 with 500nm lattice constant.
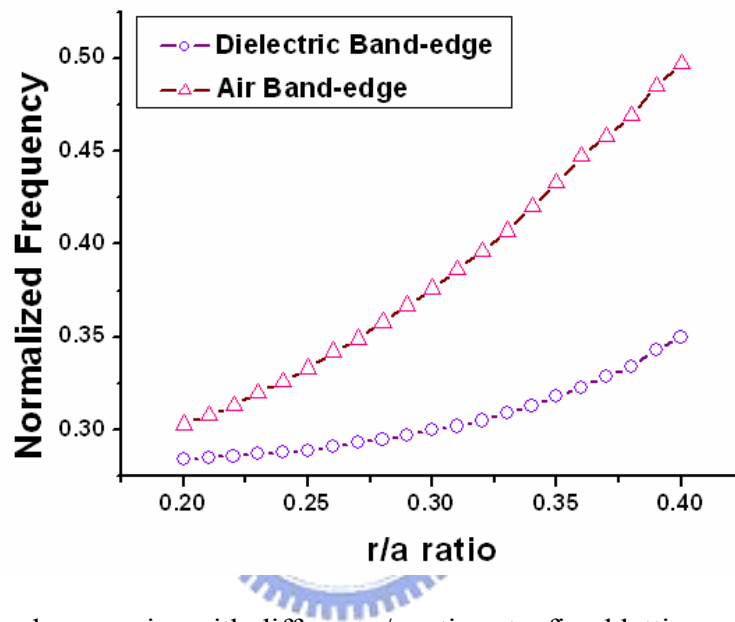

Fig. 2-4. The band-gap varies with different r/a ratios at a fixed lattice constant.

A good alignment between the PL spectrum and the photonic band-gap with 0.28 r/a ratio is shown in Fig. 2-6. In this figure, the position of the peak of PL spectrum is in the middle of the band-gap. In addition, the span of the measured PL spectrum is about 200nm and the width of the band-gap is 0.063 in normalized frequency which is corresponding to 300 nm span in wavelength from 1395nm to 1695nm. There is sufficient spectrum range for the resonances of micro-cavities. However, as we will see in the next section, the lasing properties will be affected significantly by the alignment between the gain peak of MQWs and the resonance modes instead of that between the gain peak of MQWs and the band-gap.
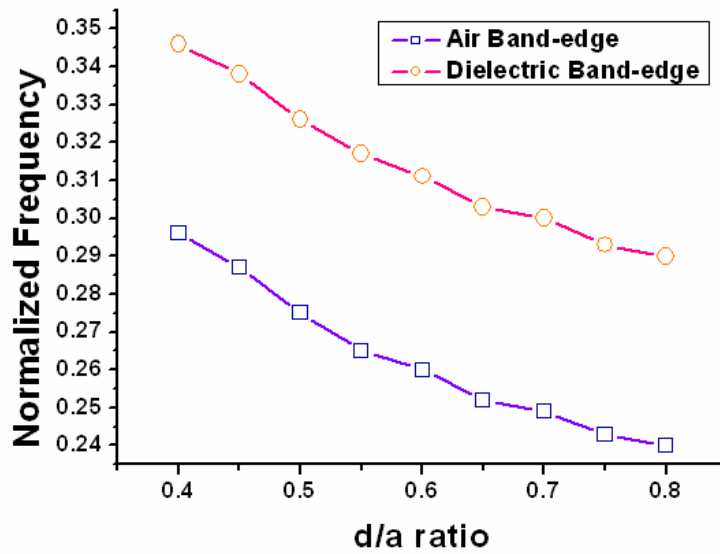
Fig. 2-5. The band-gap varies with different d/a ratios at a fixed lattice constant and r/a ratio.
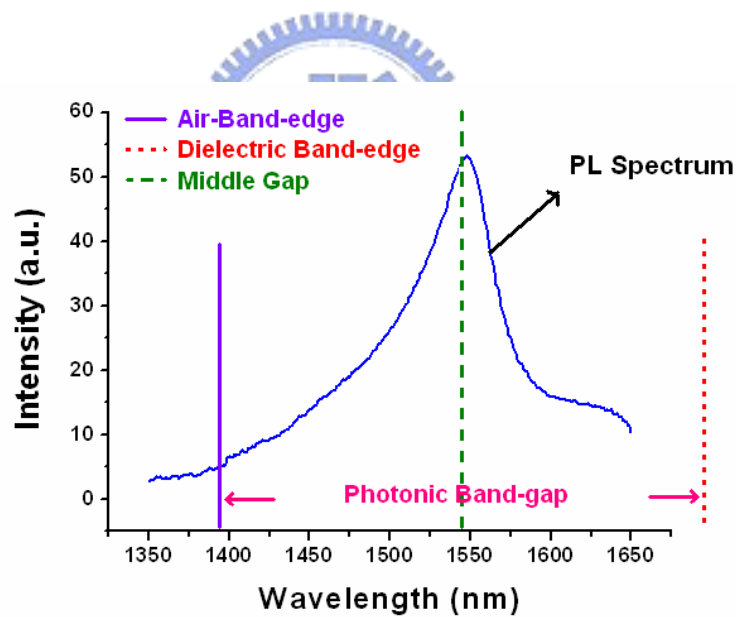

Fig. 2-6. A good alignment between the PL spectrum and the photonic band-gap. The PL spectrum peak lies in the middle of the band-gap. The r/a ratio for the photonic crystal pattern is 0.28 with 500nm lattice constant.

The index profile of the asymmetric structure is shown in Fig. 2-7. In this structure, the lattice constant 400nm is used because of the higher index of sapphire substrate than that of

the air-cladding. The band diagram of TE-like bands below the light line is shown in Fig. 2-8. There will be more optical loss in the sapphire substrate side due to the smaller index contrast [18]. The lattice constant and the r/a ratio are 400nm and 0.28. The width of band-gap is about 0.03 in normalized frequency corresponding to 150 nm span in wavelength.
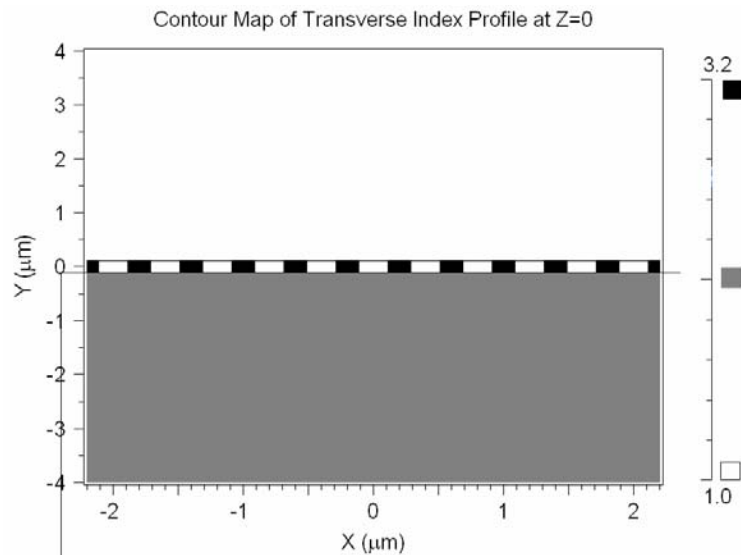

Fig. 2-7.   The index profile of the asymmetric photonic crystal slab structure.

The variation of band-gap with different r/a ratios at a fixed lattice constant is shown in Fig. 2-9. There is also a good alignment between the PL spectrum of real samples and the calculated band-gap.
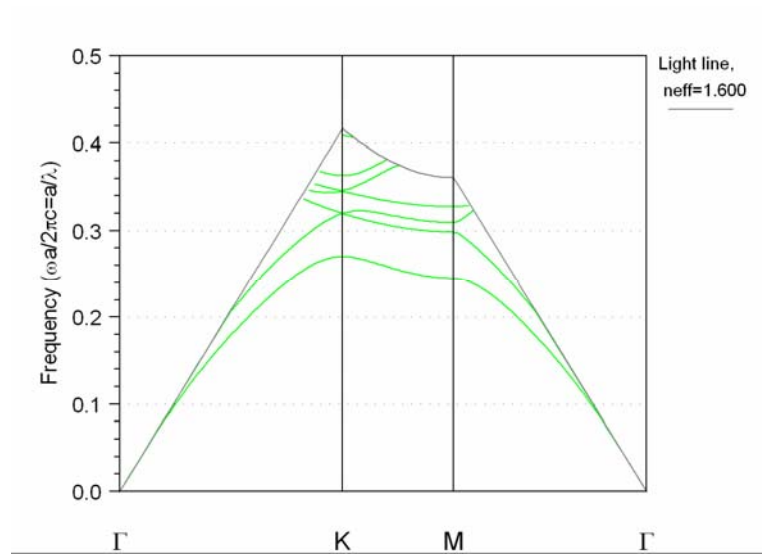
Fig. 2-8.　The typical band diagram of an asymmetric photonic crystal slab structure with 400nm lattice constant and 0.28 r/a ratio.
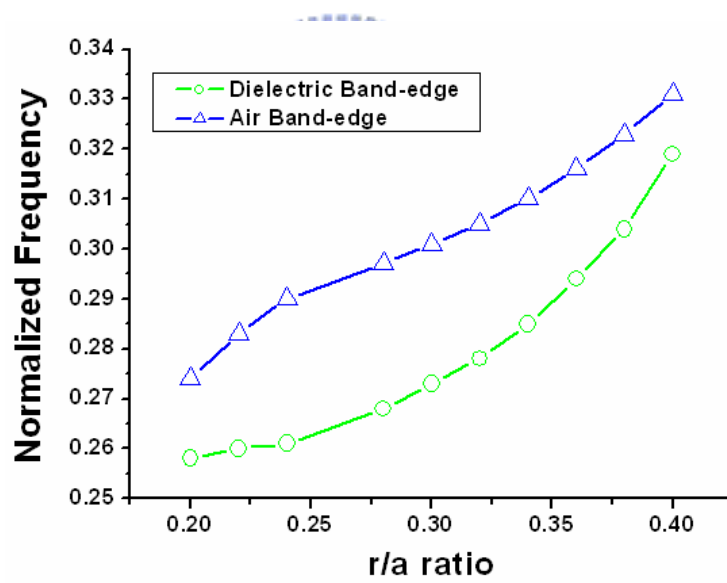

Fig. 2-9.　The band-gap varies with different r/a ratios.

2-2. Mode Analysis

In order to know more about the defect modes in photonic crystal micro-cavities, we use FDTD method to calculate the frequencies and profiles of resonance modes. In this section, we show a simulated resonance spectrum and the lasing mode profile.

A D3 photonic crystal micro-cavity with 500nm lattice constant and 0.24 r/a ratio is used in our simulation. The spectrum of resonance modes is shown in Fig. 2-10. In this spectrum, there are several resonance peaks. In fact, there should be over ten resonance modes in the band-gap. This could be caused by the large time step in our simulation setup. In addition, some parameters such as boundary conditions and launch type of the source have to be modified. The peak at 1577nm is the lasing mode in real case because of the alignment with the PL of MQWs.
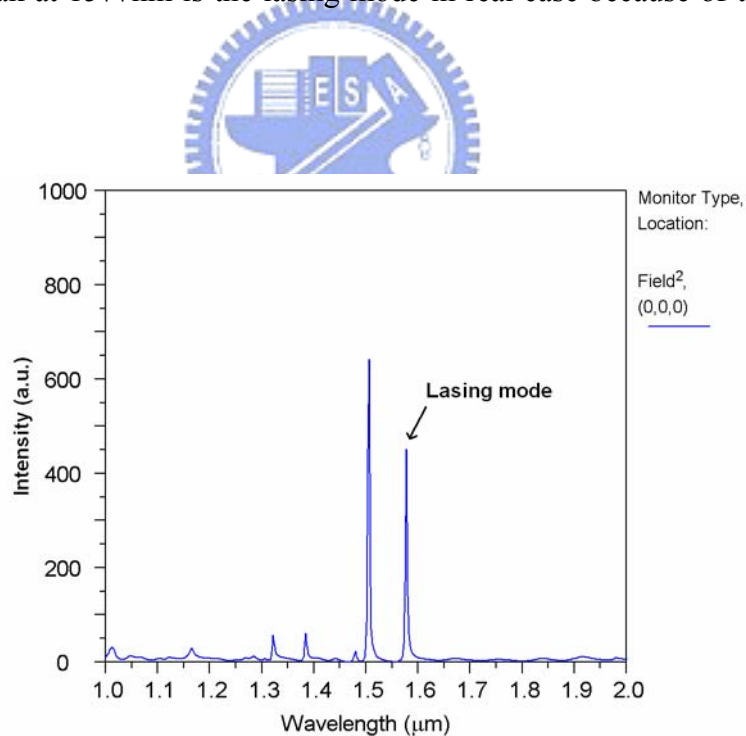

Fig. 2-10. The spectrum of resonance modes in D3 micro-cavity with 500nm lattice constant and 0.24 r/a/ratio.

The lasing mode profile at 1577nm is shown in Fig. 2-11. A hexagonal symmetry can be observed in this figure. The resolution is limited by the FDTD time step size and the detector.
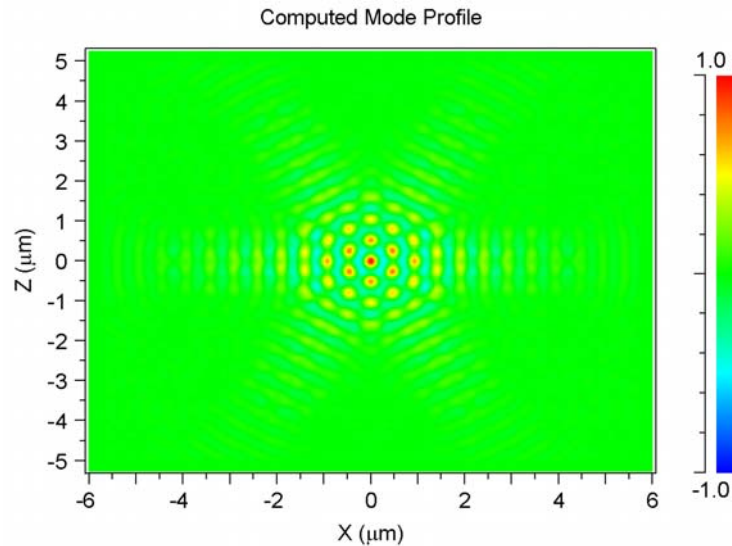

Fig. 2-11.　The lasing mode profile of the D3 cavity at 1577nm.

In our previous discussion, a good alignment between the band-gap and the gain peak of MQWs is achieved. However, we find that the high Q resonance modes are near the dielectric band instead of the middle of band-gap. As a result, one should make a good alignment between the gain peak of MQWs and the resonance modes. The lowest threshold can be achieved by aligning the highest Q resonance mode with the gain peak.

2-3. Conclusion

In this chapter, the band diagrams and the band gap variations of two-dimensional photonic crystals with different lattice parameters including lattice constants, r/a ratios, and membrane thicknesses are calculated by 3D PWE method. The resonance modes of D3 photonic crystal micro-cavity are also calculated by 2D FDTD method. The optimization of the device can be obtained by making a good alignment between the gain peak and the resonance mode with highest Q factor.

3. Fabrication of Two-Dimensional Photonic Crystal Lasers

The basic design principles have been introduced in chapter 2. In this chapter, the fabrication processes of two-dimensional photonic crystal lasers with membrane structure and sapphire-bonding structure will be introduced.

3-1. Membrane Structure

The epitaxial structure of InGaAsP/InP MQWs for membrane structure is shown in Fig. 3-1. The epitaxial wafer consists of four 10 nm 0.85% compressively-strained InGaAsP quantum wells which are separated by three 20nm unstrained InGaAsP barrier layers. It has been confirmed that the PL spectrum of the QWs is centered at 1.55 μm with 200nm span at room temperature. The 60nm InP cap layer is used to protect the MQWs during a series of dry etching processes.
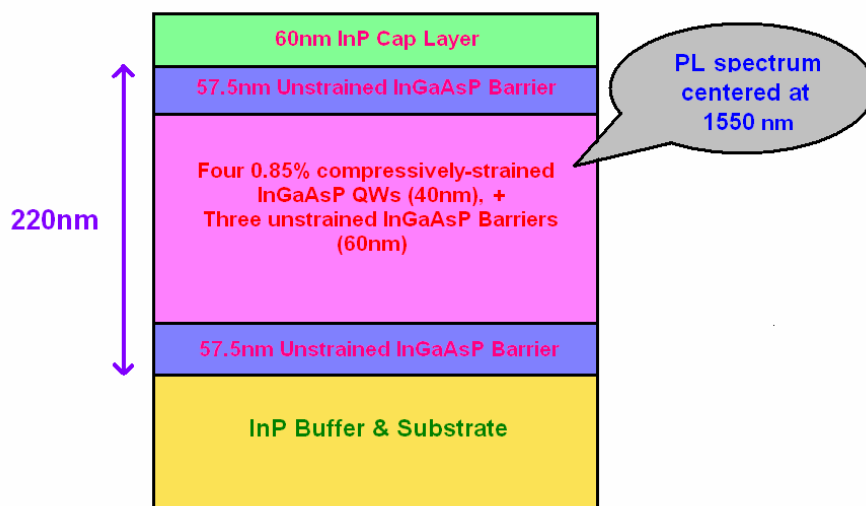

Fig. 3-1.   The epitaxial structure of InGaAsP MQWs for photonic crystal membrane lasers. The thickness of the membrane is about 220nm.

At first, a hard mask consists of 140 nm silicon-nitride is deposited on the sample using plasma-enhanced chemical vapor deposition (PECVD). Then a 240 nm polymethylmethacrylate (PMMA) layer is spun on the sample by a spin coater. The photonic crystal pattern is defined on the PMMA layer using electron beam writer. The process flow of this part is illustrated in Fig. 3-2.
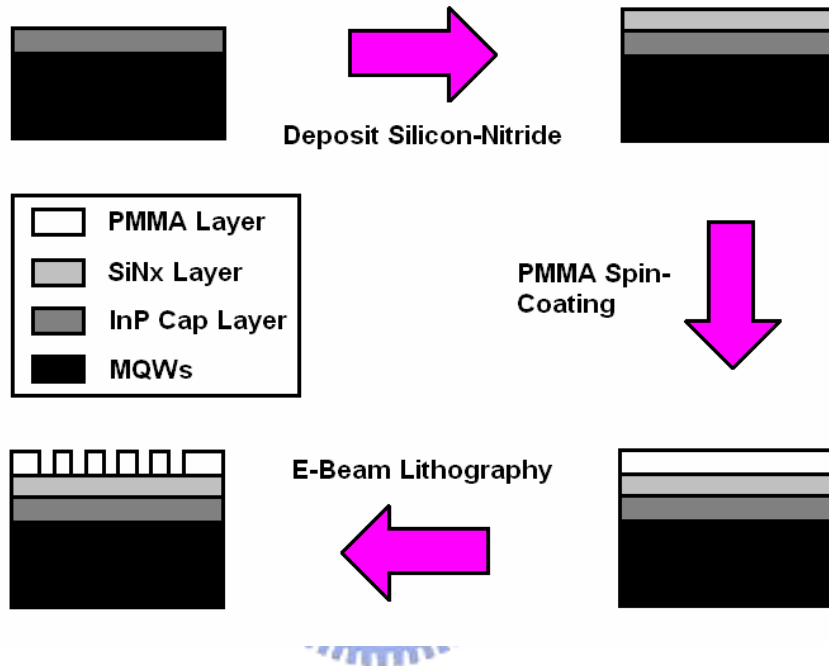

Fig. 3-2.   The first part of photonic crystal membrane lasers fabrication process.

The patterns can be observed in scanning electron microscopy (SEM) as shown in Fig. 3-3 after a series of development and fixation processes. The radius and the shape of the air-holes are a little enlarged and distorted from the original design. This can be improved by choosing proper dosages. The pattern is transferred to silicon-nitride layer by using Reactive-Ion-Etching (RIE). Then the residual PMMA layer is removed by O_2 plasma. After the PMMA layer is removed, the pattern is transferred to MQWs layer by Inductively-Coupled-Plasma (ICP) etching process at $150^{\circ}C$. The cross-section after ICP etching is shown in Fig. 3-4. The silicon-nitride hard mask is then removed. The finished photonic crystal patterns after these etching steps are shown in Fig. 3-5.
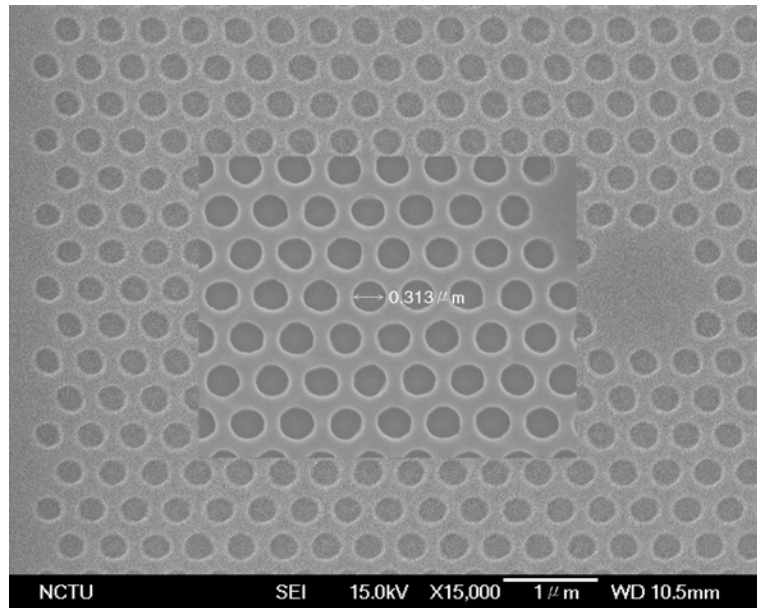
Fig. 3-3. Top view SEM picture showing the photonic crystal patterns defined on the PMMA layer. The enlarged air hole radius can be attributed to the over-exposure during electron-beam lithography process.
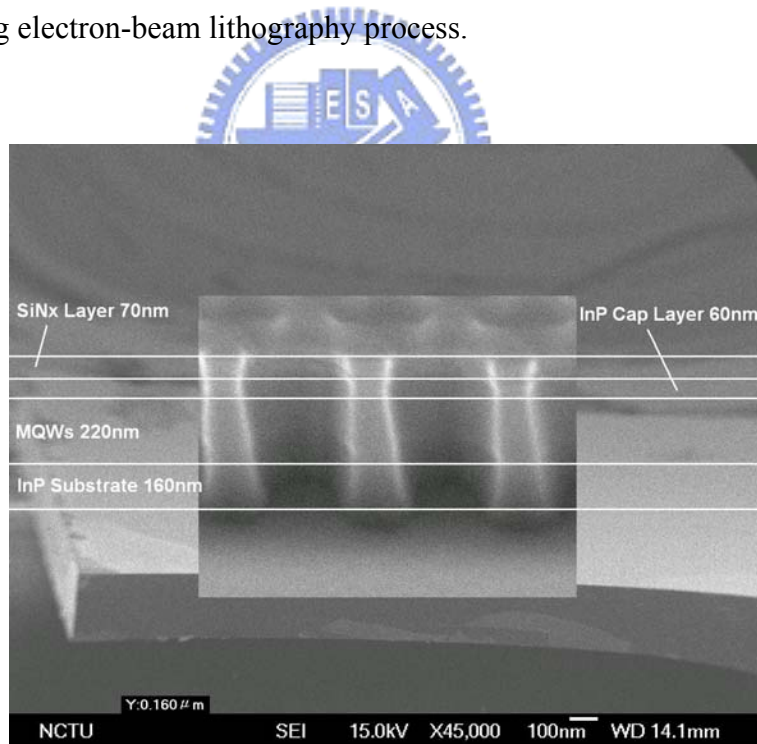

Fig. 3-4. The cross section SEM picture of the photonic crystal patterns transferred to MQWs layer. The air holes are over-etched 160nm to InP substrate.
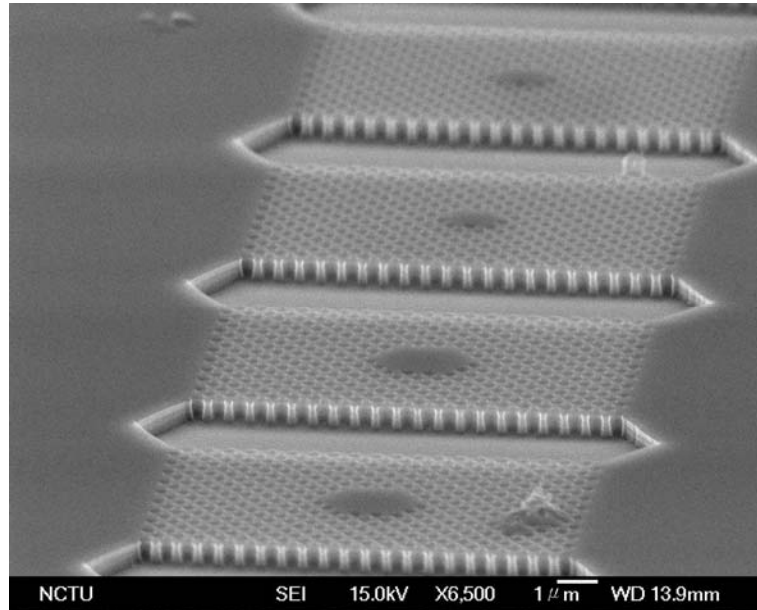
Fig. 3-5. SEM picture of photonic crystal patterns transferred to MQWs by dry etching processes. The micro-cavities can be observed in the SEM picture.

In order to fabricate the membrane structure, the InP substrate below the MQWs should be removed. The undercut can be constructed by using a mixture of HCl and water. This process also removes the 60 nm InP cap layer and smoothes the surface and the sidewall of the air-holes. This process could be also regarded as a gentle wet etching process to reduce the scattering, i.e. optical loss, caused by the surface roughness. The wet etching process is anisotropic. The wet etching stops at 95° and 40° from <-1, 0, 0> direction in the (0, -1, -1) plane and the (0, 1, -1) plane [19] as shown in Fig. 3-6 and Fig. 3-7. The undercut trench under the photonic crystal pattern can be formed for the larger air holes. For smaller air holes, the wet etching results in a small wedge-shape undercut in each photonic crystal hole. For smaller air holes, the small wedges under every hole have no chance to meet each other. As a result, no undercut trench can be formed.
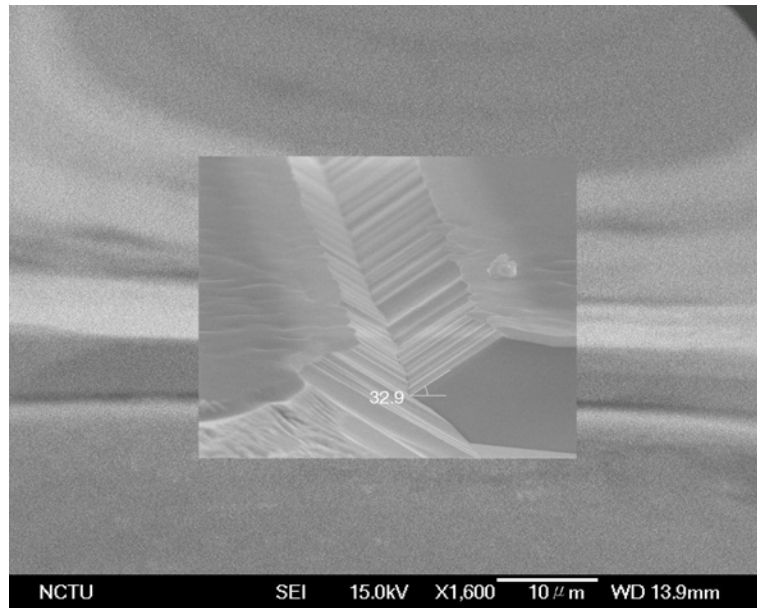
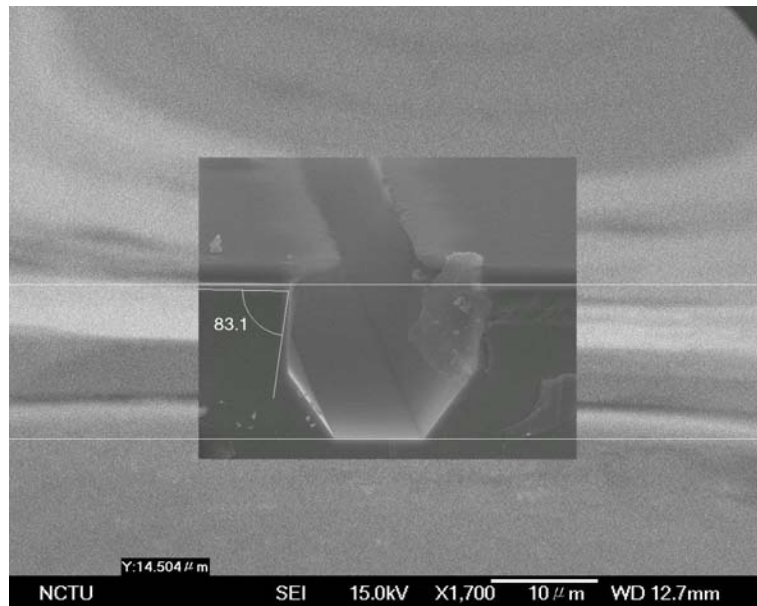Fig. 3-6. There is a 40° etching stop plane in (0, 1, -1) direction of InP materials.

Fig. 3-7. There is a 95° etching stop plane in (0, -1, -1) direction of InP materials.

In order to solve this problem, a window between two components is necessary. The opening of the window can prevent the wet etching of the air holes from stopping, and then a two-dimensional photonic crystal membrane structure is completed. A significant V-shaped undercut trench can be observed in Fig. 3-8 and Fig. 3-9. The overview of the fabrication process is shown in Fig. 3-10.
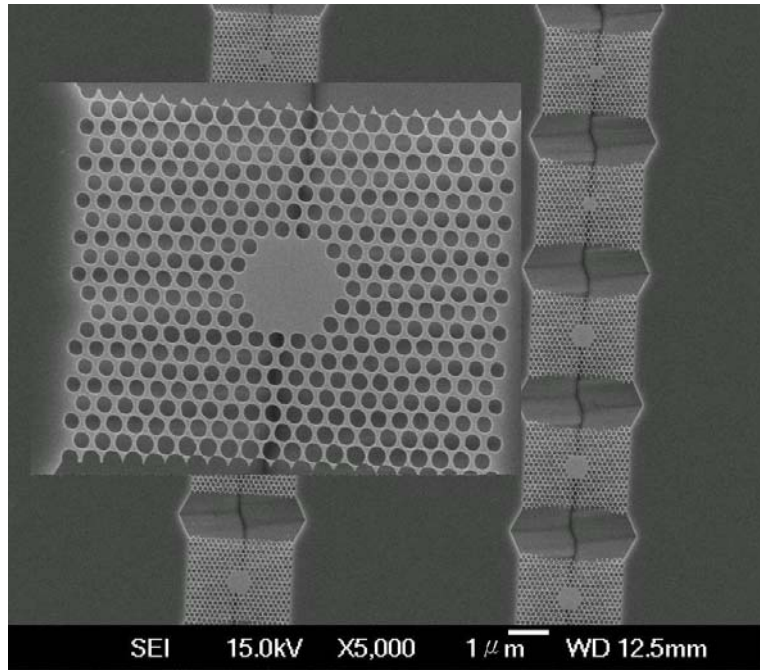
Fig. 3-8.   The top-view of two-dimensional photonic crystal membrane laser arrays. Our

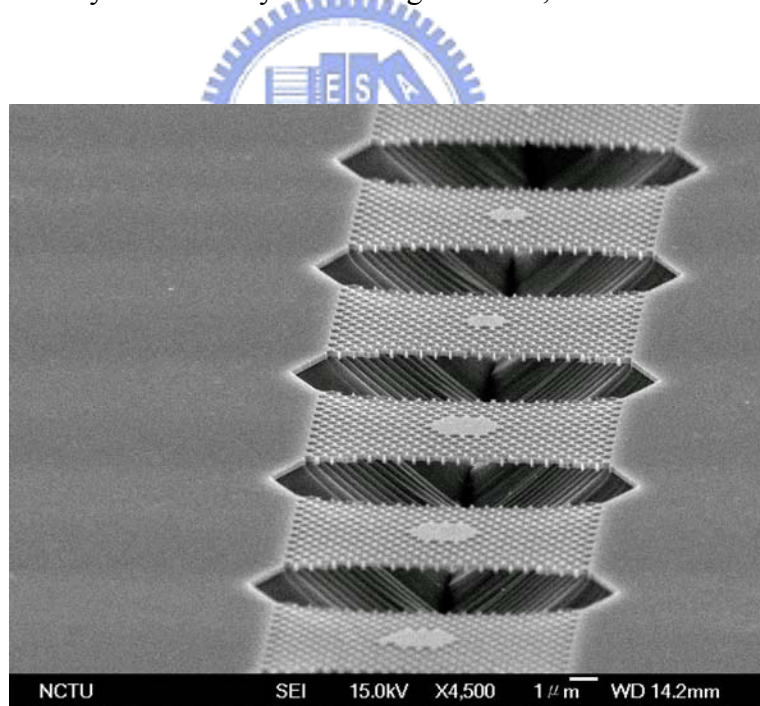micro-cavity is formed by 19 missing air-holes, i.e. D3 micro-cavity.

Fig.3-9. The tilted view SEM picture of a two-dimensional photonic crystal laser array. The

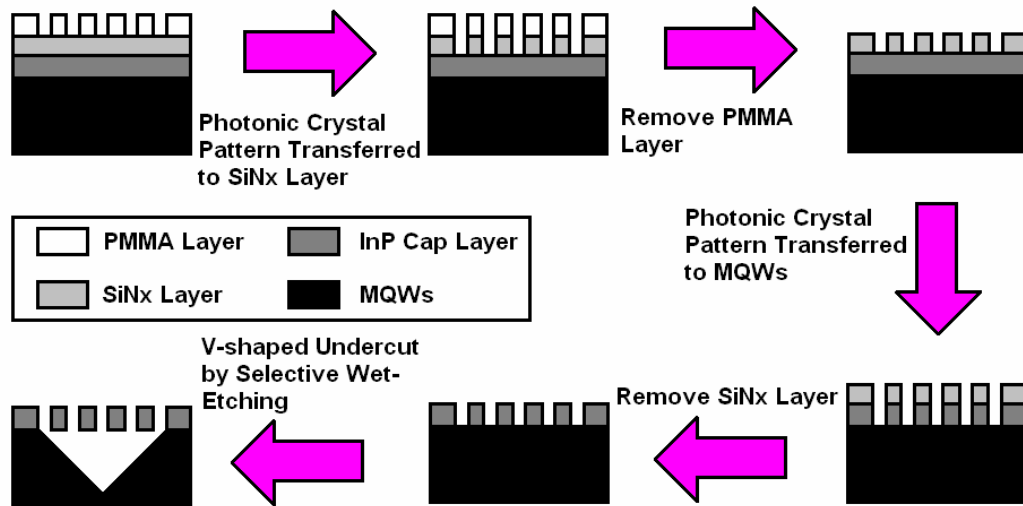V-shaped undercut trench and the membrane structure can be seen clearly.

Fig. 3-10. The overview of fabrication process of two-dimensional photonic crystal membrane lasers.

3-2. Asymmetric Structure

As we mentioned before, we can replace the air-cladding by sapphire substrate with better thermal conductivity in order to improve the heat dissipation problems in membrane structure. In order to integrate sapphire with InGaAsP material, bonding technology is required. In this section, I will introduce two different fabrication processes to fabricate the asymmetric structure of two-dimensional photonic crystal lasers. One is wafer-bonding, and the other is glue-bonding.

3-2-1. Wafer-Bonding

The epitaxial structure of MQWs wafer for wafer bonding is shown in Fig. 3-11. This structure is similar to the epitaxial structure for membrane fabrication. The main difference is the 40nm InGaAs etching stop layer above InP substrate. It is used to protect the MQWs during the InP substrate wet etching.
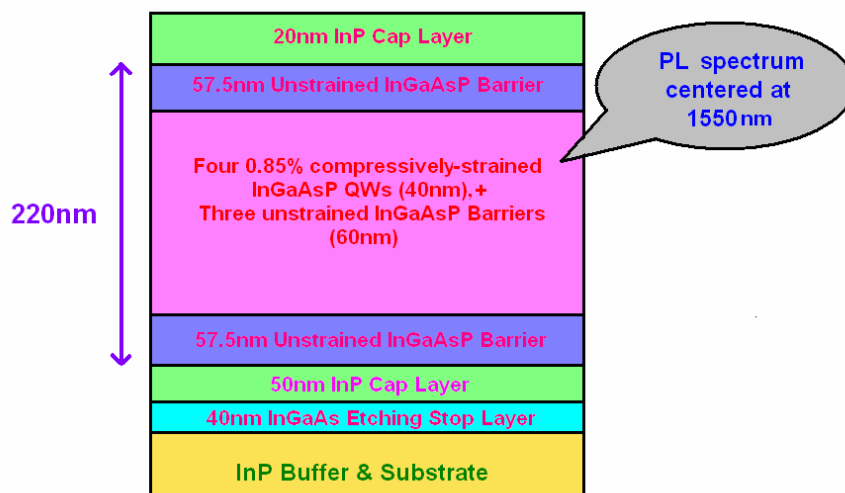

Fig. 3-11. The epitaxial structure of InGaAsP MQWs for wafer-bonding process.

This technology is used to bond InGaAsP layer with the sapphire substrate together. Before we bond them together, the 20nm InP cap layer should be removed. And then the sample is wafer-bonded to the sapphire substrate by using direct wafer bonding technology in a H₂ environment at 450°C. The 330μm InP substrate and 20nm etching stop layer will be removed after the wafer-bonding process. At last, the 50nm InP cap layer is also removed. The remaining process is the same with that for membrane structures. An overview of above fabrication process is shown in Fig. 3-12.
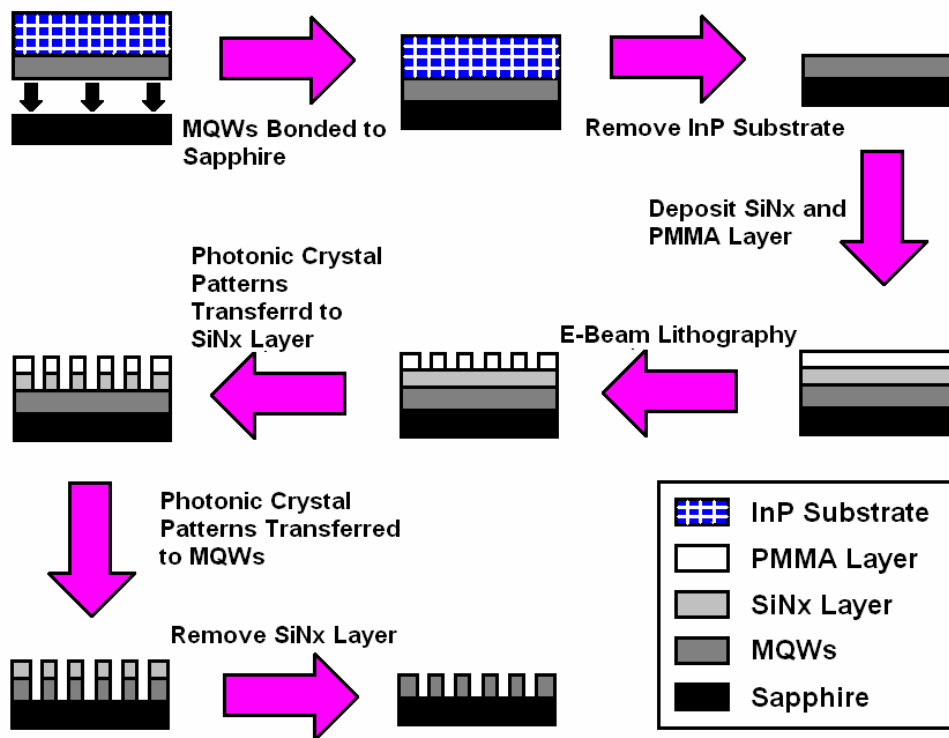

Fig. 3-12.   An overview of fabrication process of asymmetric structure with sapphire substrate.

3-2-2. Glue-Bonding

The other way to fabricate this asymmetric structure is presented in this sub-section. At first, we use the same method to remove the InP cap layer. And then we use glue bonding technology which is more direct and simpler than wafer-bonding. The InP substrate and etching stop layer are also removed after the glue bonding process. The most significant difference between wafer-bonding and glue-bonding is the temperature restriction during the following dry etching steps. The glue-bonding sample can not sustain the temperature higher than 80°C. As a result, the ICP process can not be used in this case.

A brand new fabrication process is setup by using focused-ion-beam (FIB) system. It solves the temperature problem and provides a very simple fabrication process. The photonic crystal pattern is patterned directly by focused gallium ion beam without any masks. The top-view and tilted-view of the finished device are shown in Fig. 3-13 and Fig. 3-14. However, there are still problems. First, the sidewall of the air-holes is not vertical. This would increase extra optical loss of the device. Second, the gallium residue on the membrane surface would affect the emission efficiency of our devices. These problems should be solved in the future. An overview of this fabrication process is shown in Fig. 3-15.
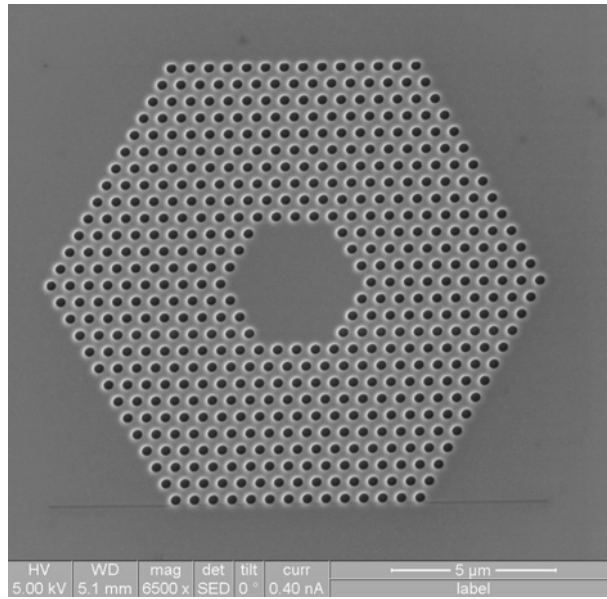
HV	WD	mag	det	tilt	curr	
5.00 kV	5.1 mm	6500 x	SED	0 °	0.40 nA	5 µm
						label

Fig. 3-13. The SEM picture of top view of the asymmetric photonic crystal laser structure after FIB process.

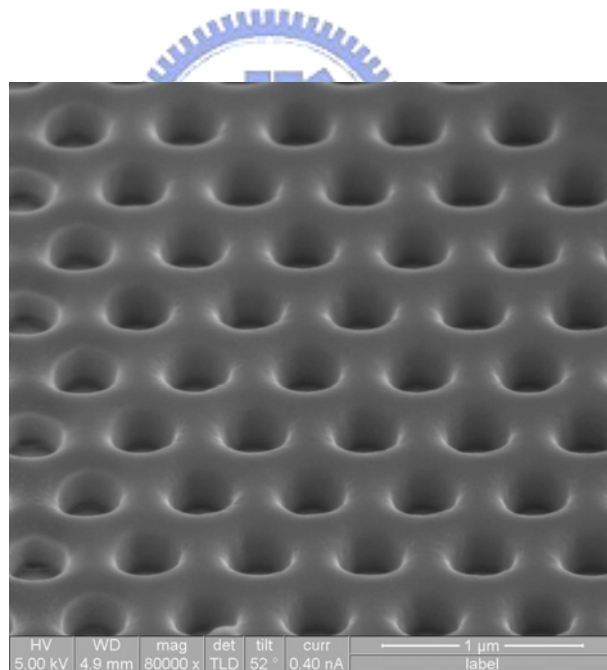| HV	WD	mag	det	tilt	curr	
5.00 kV	4.9 mm	80000 x	TLD	52 °	0.40 nA	1 µm
						label

Fig. 3-14. The SEM picture of the asymmetric photonic crystal laser structure with a tilt angle.
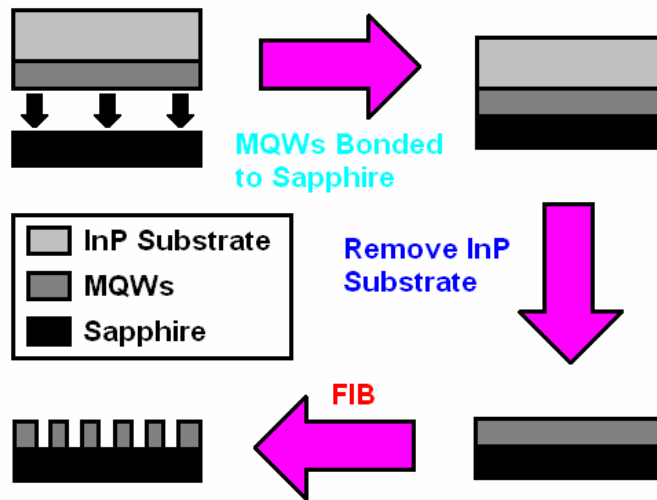
Fig. 3-15.   An overview of fabrication process of asymmetric photonic crystal laser structure

using glue-bonding technology and the FIB systems.

3-3. Conclusion

In this chapter, the fabrication processes of membrane and asymmetric structures of two-dimensional photonic crystal lasers are introduced. Photonic crystal patterns on are defined by e-beam lithography and a series of dry etching process. The membrane structure is formed by HCl selective wet etching. The asymmetric structure is fabricated by two different processes. One is wafer-bonding and ICP dry etching, and the other is glue-bonding and FIB etching.

# 4. Measurement Results and Analysis

4-1. Measurement Setup

In order to measure the characteristics of the epitaxial materials and two-dimensional photonic crystal micro-cavities, a micro-PL system with sub-micrometer-scale resolution in space and sub-nanometer-scale resolution in spectrum is necessary. The simple configuration and photo of our micro-PL system are shown in Fig. 4-1(a) and (b).
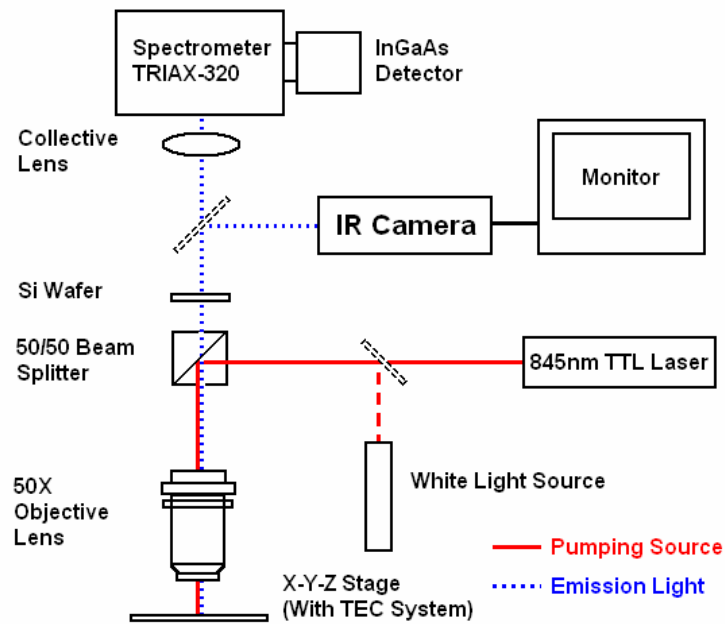
(a)
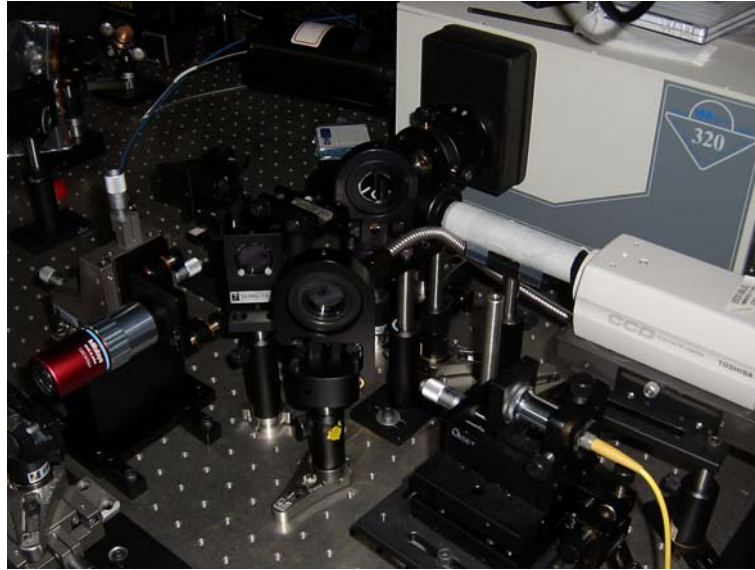
(b)

Fig. 4-1.　(a) The configuration of micro-PL system. (b) The photography of the system.

In this system, an 845 nm TTL laser is used as the pump source. This TTL laser can be used both under pulse operation and continuous-wave operation. In pulse operation case, we use a function generator to generate a pulse signal in order to modulate its driving current, and then the output laser light will be under pulse operation. In continuous-wave operation case, the function generator is turned off and a short circuit is formed. In this case, the driving current is not modulated. The basic ideas of these two operations are illustrated in Fig. 4-2. All pump conditions we used in our experiments are listed in Table 4-1. In addition, its output profile is shaped to a circle by its module. And a low divergence output beam is benefit for setting the optical path of the system.

The pump beam is reflected into a 50x long working distance NIR objective lens which is mounted on a 3-axis stage with numerical aperture of 0.5 by a 50/50 beam splitter. The 48% reflection in angle 45° of the beam splitter for 845 nm wavelength is confirmed before we use it. And then the pump beam is focused to a spot with 3.5 μm to 4μm in diameter by

the objective lens. Such pump spot size is a little larger than our micro-cavity size, which is necessary. This will be explained in details in the next section.
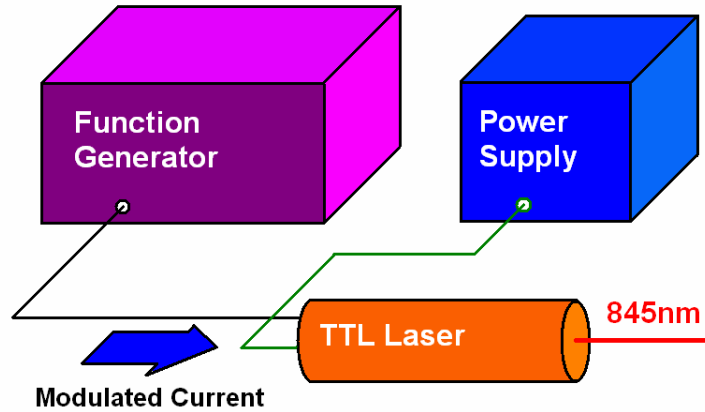

Fig. 4-2. Two operation modes of the TTL laser. The TTL laser is pumped by a power supply and the driving current is modulated by a function generator. A short circuit is formed without any modulation under continuous-wave operation when we turn off the function generator.
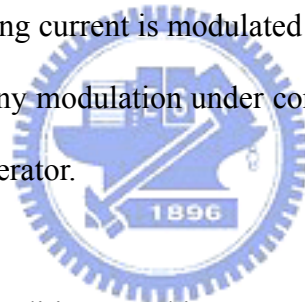
Table. 4-1. Different pump conditions used in our experiments.

Pulse Width (ns)	Repetition Rate (MHz)	Duty Cycle (%)
20	0.5	1.0
30	0.5	1.5
40	0.5	2.0
50	0.5	2.5
60	0.5	3.0

There is a simple microscopic function in this micro-PL system. When mounting our sample on a high resolution 3-axis stage, we can know the positions of our micro-cavity and the pump light spot exactly from the monitor by a luminescence system with a white light source and the CCD camera as shown in Fig. 4-3, which is captured by a digital camera. In this picture, the image of a photonic crystal laser array is shown clearly. One can see the

positions of the micro-cavities and the 845nm pump beam spot with 3.5 to 4 μm in diameter. The pump spot is aligned quite well with our micro-cavity.
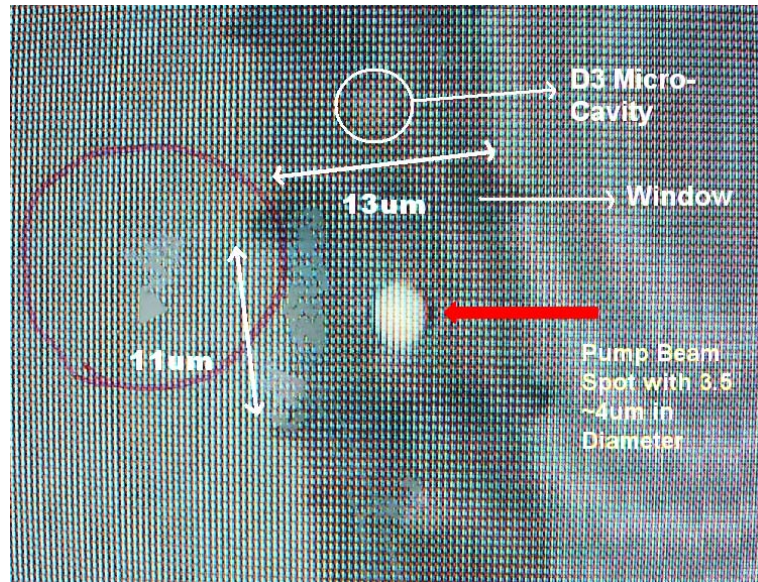

Fig. 4-3.   The image of a two-dimensional photonic crystal laser array captured from the monitor. One can see the positions of the micro-cavities and the windows between two components. The 845nm pump beam is focused on the micro-cavity.

The objective lens collects the output light from the top of the sample. A silicon wafer is put after the beam splitter in order to block the reflected pump light. We use a collective lens to focus the output signal into the slit of our spectrum analyzer, TRIAX-320, with 0.12 nm resolution. An InGaAs detector with good responsibility from 900nm to 1600nm is used to obtain the lasing spectra of our devices. We also use this system to characterize the PL spectrum of the epitaxial materials. In order to obtain a better S/N ratio, we setup a lock-in system in the micro-PL system. A chopper and a lock-in amplifier connected to the SAQ of TRIAX-320 are used. A typical PL spectrum of our InGaAsP MQWs is shown in Fig. 4-4.
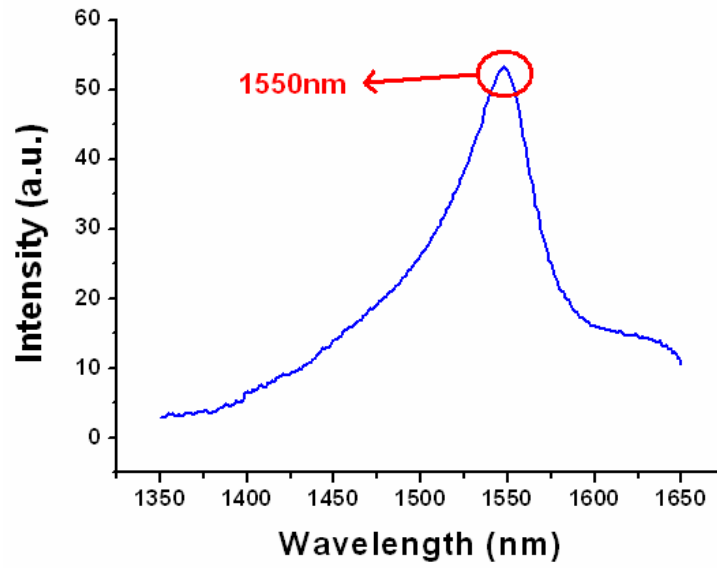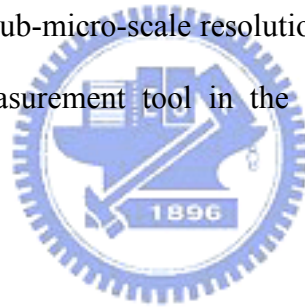
Fig. 4-4.   A typical PL spectrum of our MQWs. It is centered at 1550nm with 200nm span.

A micro-PL system with sub-micro-scale resolution microscopic function has been setup. This is a very important measurement tool in the researches of photonic crystal active devices.

4-2. Basic Lasing Characteristics

In this section, I will show some basic characteristics of two-dimensional photonic crystal lasers including L-L curve, lasing spectrum, mode polarization, and wavelength tuning properties. All measurements are done at room temperature by our micro-PL system.

The lasing spectrum well above threshold of a typical two-dimensional photonic crystal laser with 2% duty cycle at 0.5MHz repetition rate is shown in Fig. 4-5(a). Its lasing wavelength is 1590.2nm and full-width half-maximum (FWHM) is 0.3nm which are limited by the resolution of our spectrum analyzer. Its side mode suppression ratio (SMSR) is larger than 19dB above threshold. The lasing spectrum near threshold is shown in Fig. 4-5(b).
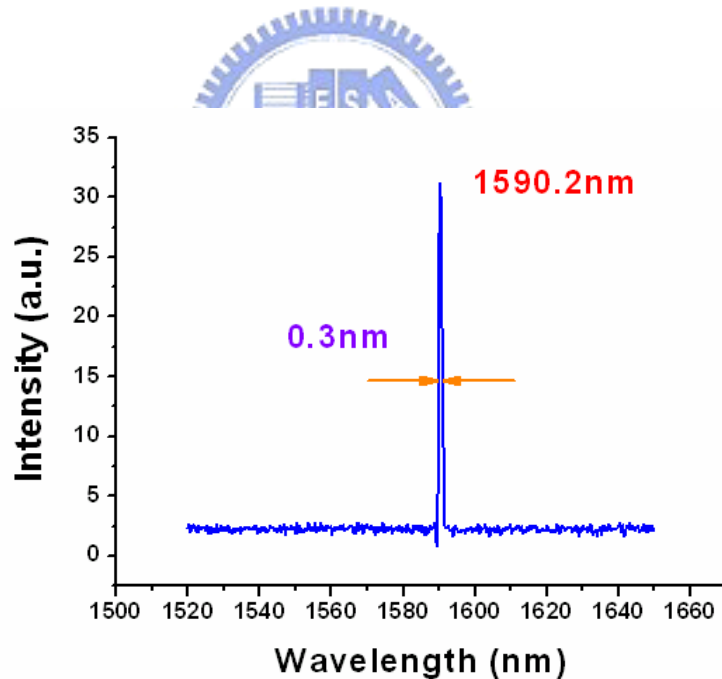
(a)
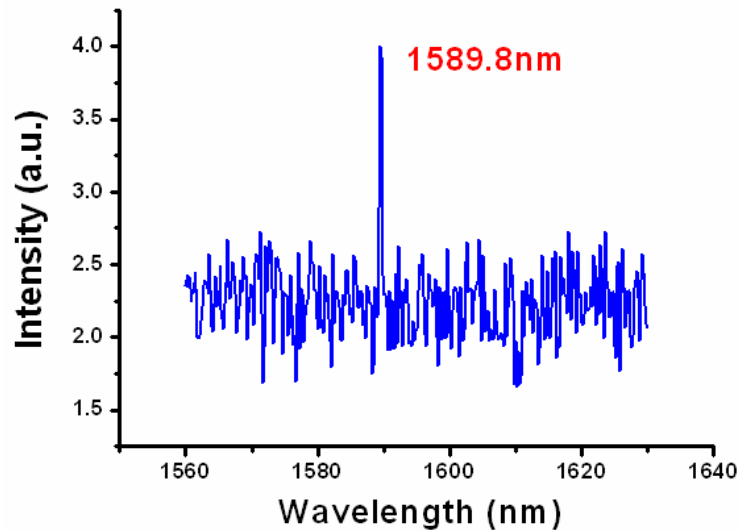
(b)

Fig. 4-5.   The typical lasing spectra (a) above threshold and (b) near threshold of a two-dimensional photonic crystal laser.

The L-L curve of a typical two-dimensional photonic crystal laser pumped with the same condition is shown in Fig. 4-6. The threshold average pump power is about 5.6 µW. In addition, the pump spot size with 3.5µm to 4µm in diameter, which is larger than the area of the micro-cavity, is used to pump the surrounding area of the micro-cavity to transparency, and then the additional absorption by the surrounding area can be reduced.

We also measure the lasing spectrum above threshold which is shown in Fig. 4-7. The lasing peak is saturated because of purpose to observe the side modes. The most significant side mode is centered at the wavelength 20nm shorter than the lasing peak. A method to reduce the intensity of this side mode to increase the SMSR has been reported [20].
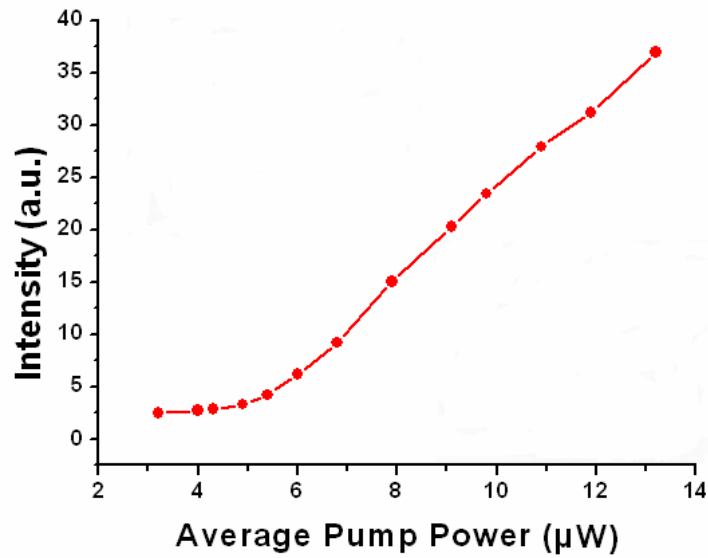
Fig. 4-6. The L-L curve of a two-dimensional photonic crystal laser. The threshold is estimated to be 5.6μW in average pump power.
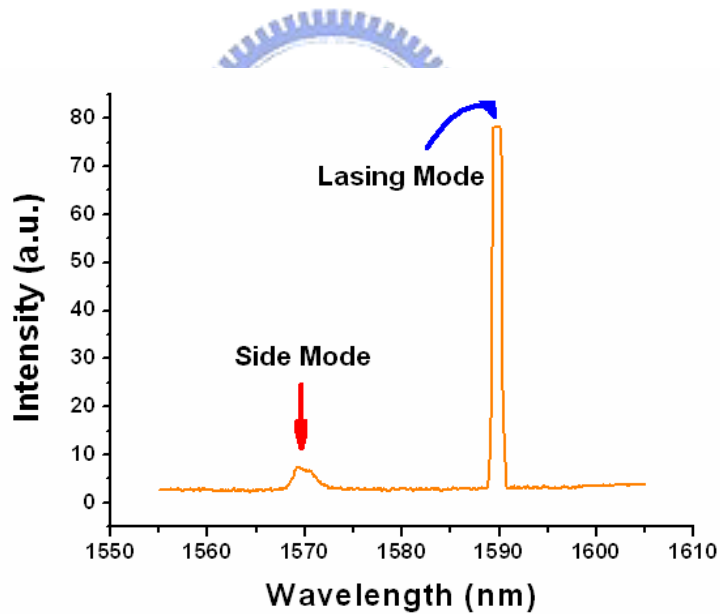
Fig. 4-7. There is a significant side mode at the wavelength 20nm shorter than the lasing wavelength.

In fact, there are tens of resonance modes in our micro-cavity with D3 cavity size. Over ten resonance modes pumped with 1.5x threshold power are shown in Fig. 4-8, which matches with the reported simulation results quite well [21]. As one can see, the intensity of

these modes is approximately proportional to the intensity of the PL spectrum of MQWs, i.e. the alignment with the gain peak of MQWs. There is red shift between the PL spectrum and the resonance modes intensity, this may caused by the high temperature in the micro-cavity region. We do not observe any resonance mode after 1600nm in wavelength. This could be attributed to the weak PL spectrum of MQWs and the bad responsibility of our InGaAs detector in the wavelength range larger than 1600nm.
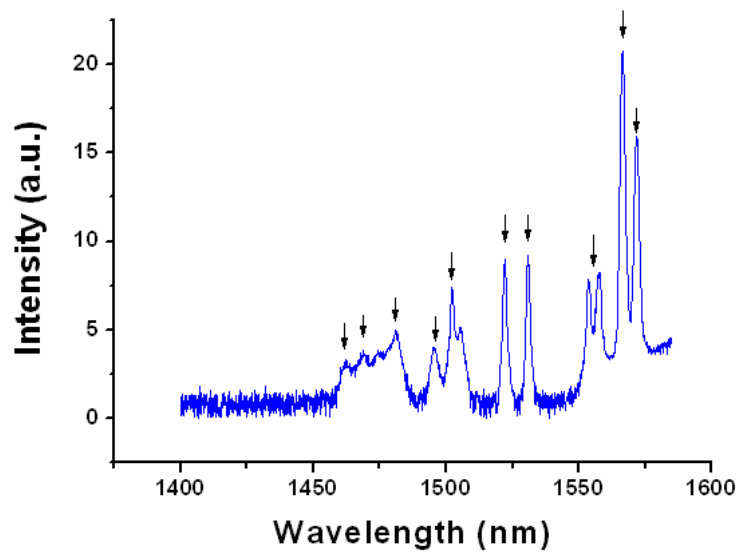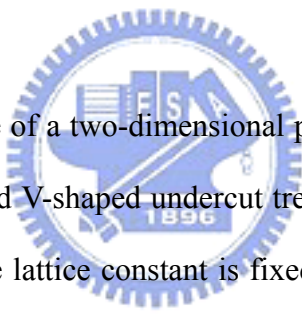

Fig. 4-8.   There are over ten resonance modes observed in the D3 photonic crystal micro-cavity.

4-3. Wavelength Tuning

As we mentioned in chapter 1, the two-dimensional photonic crystal lasers could be an attractive and potential light source in WDM systems. In my thesis, I will introduce two methods of tuning lasing wavelength of two-dimensional photonic crystal lasers for the WDM system requirements. The first method is varying lattice parameters of the photonic crystal patterns such as the r/a ratio and the lattice constant. An array will be fabricated in this case. The second method is the thermal tuning of lasing wavelength without changing any parameters of the photonic crystals. The wavelength tuning is achieved by the index change caused by increasing temperature and this will be investigated both in experiments and theory in the next section. I would like to introduce the first one in this section.

The top view SEM picture of a two-dimensional photonic crystal laser array is shown in Fig. 4-9. The micro-cavities and V-shaped undercut trench can be observed clearly. In such a photonic crystal laser array, the lattice constant is fixed in each component and the radius of the air holes is different from each other. An overview of the measured laser arrays is shown in Fig. 4-10. The lattice constant is fixed at 500nm in all arrays, and the different radii of air holes in each array leads to different r/a ratios. It is obvious that the lasing wavelength will change with the shifting of band-gap caused by different r/a ratios. The defect modes and the band-gap will be shifted to the higher normalized frequency when there is more low-index material and vice versa.
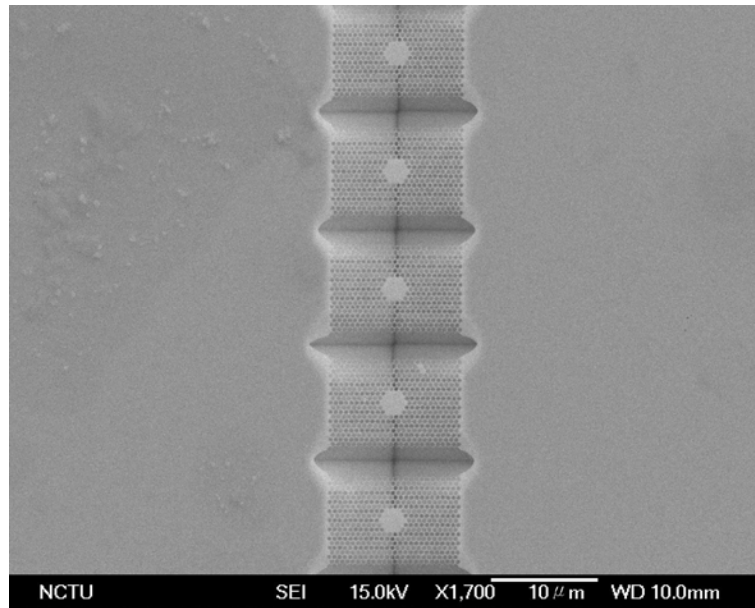
Fig. 4-9.　The top view SEM picture of a two-dimensional photonic crystal laser array.
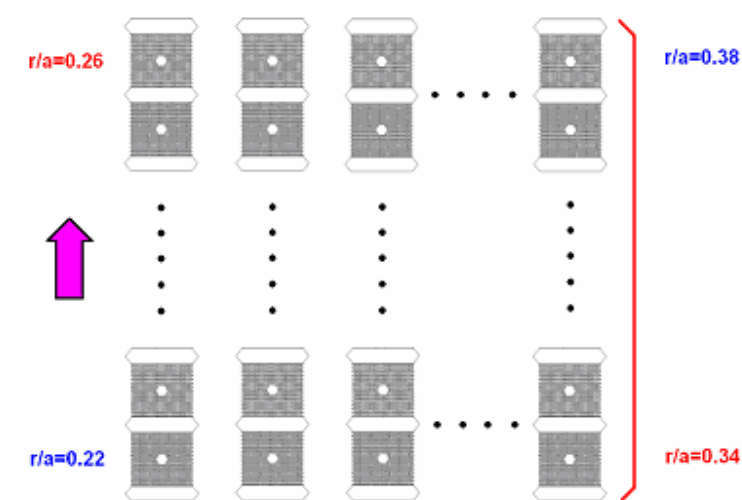
Fig. 4-10.　The two-dimensional photonic crystal laser arrays. The lattice constant is fixed at 500nm. The r/a ratio is varied from 0.22 to 0.38.

The lasing wavelengths of one photonic crystal laser array are shown in Fig. 4-11. The r/a ratio is varied from 0.26 to 0.22. The lasing wavelength increases when the r/a ratio decrease. The total wavelength variation is about 22nm. In this figure, the nonlinear increasing of lasing wavelength can be attributed to the imperfect fabrication process.
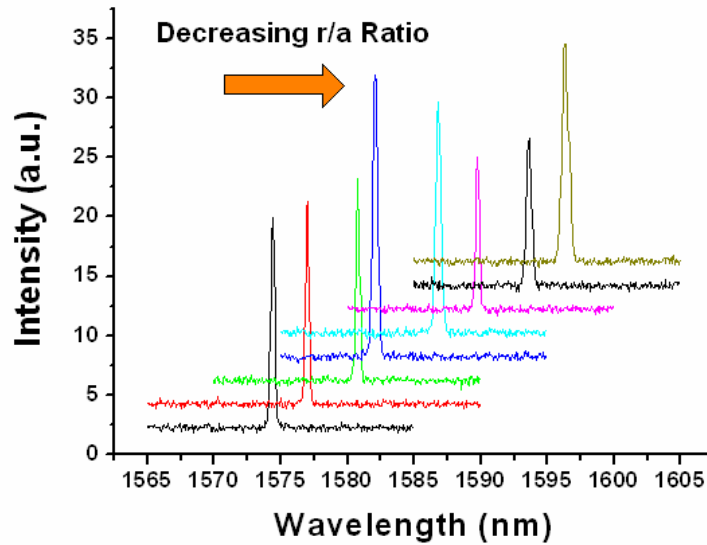
Fig. 4-11. The lasing wavelengths of one photonic crystal laser array. There is a red shift in lasing wavelength due to decreasing r/a ratio. The intensity of each lasing wavelength is shifted on purpose in order to distinguish them more easily.

We also measure photonic crystal laser arrays of different lattice constants with a fixed r/a ratio. An overview of the measured laser arrays is shown in Fig. 4-12. The r/a ratio varies from 0.27 to 0.37 in each array and the lattice constant varies from 470nm to 580nm in 10nm increment. The lasing wavelength can be tuned by different lattice constants with a fixed r/a ratio. The lasing wavelengths of one laser array with a fixed r/a ratio 0.35 and different lattice constants are shown in Fig. 4-13. The lasing normalized frequency is approximately fixed at 0.34. One can see that there are "mode hopping" in the range of the lattice constant we measured. This phenomenon is caused by the variation of the alignment between the PL gain peak and the resonance modes.
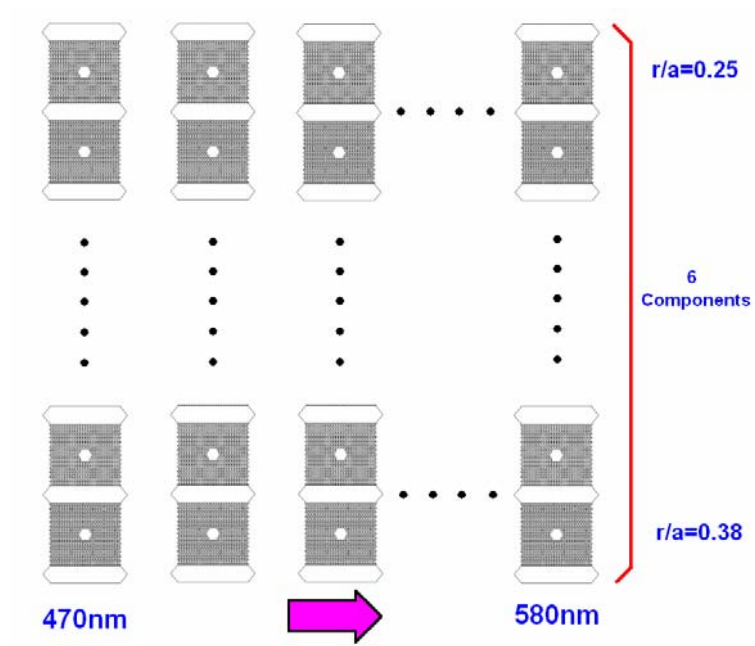
Fig. 4-12. The photonic crystal laser arrays with different r/a ratios from 0.27 to 0.37 and

lattice constants from 470nm to 580nm.
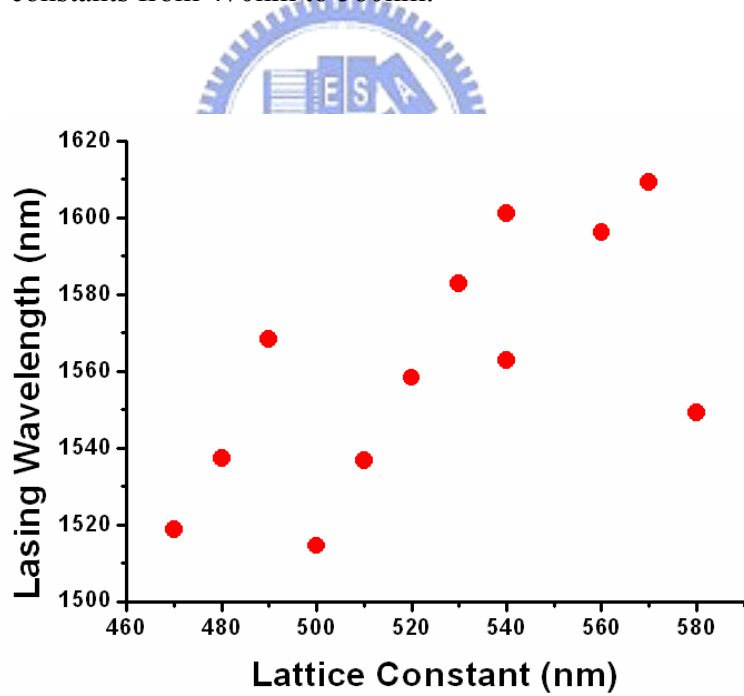
Fig. 4-13.　The lasing wavelength tuning caused by different lattice constants.

4-4. Thermal Analysis

As we mentioned before, lacking a good heat sink in the membrane structure of two-dimensional photonic crystal lasers leads to serious thermal effects which are similar to that of conventional semiconductor lasers. In this section, I would like to investigate the thermal effects of two-dimensional photonic crystal lasers. These analyses could be good references or guidelines in achievement of continuous-wave operation of two-dimensional photonic crystal lasers.

First of all, a significant broadening of the lasing spectrum caused by increasing pump power or/and duty cycle can be easily observed as shown in Fig. 4-14 (a) and (b).

(a)
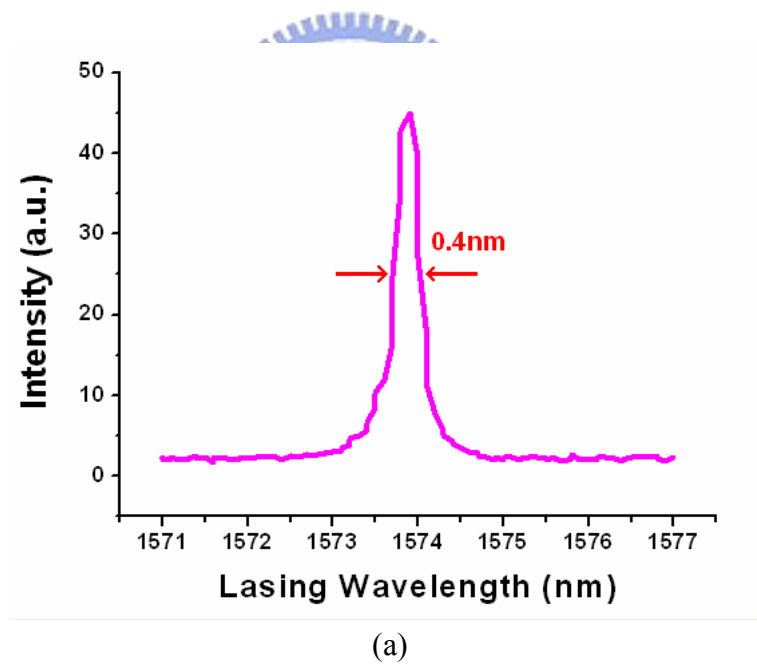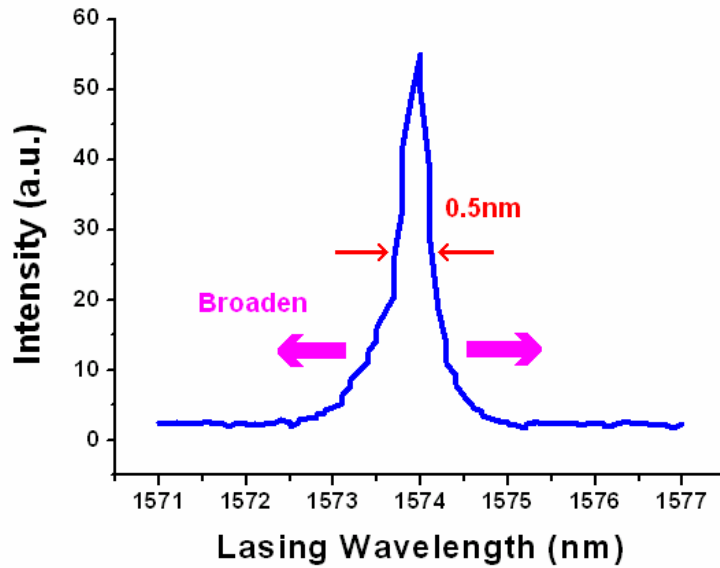
(b)

Fig. 4-14. The lasing spectra pumped by different condition with (a) lower and (b) higher duty cycles. There is about 0.5% duty cycle difference between the two pump conditions.
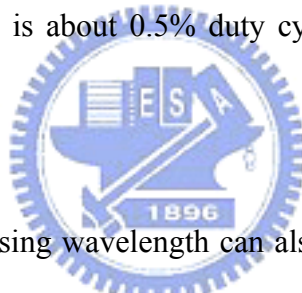
In addition, red shift of lasing wavelength can also be observed. The red shift of lasing wavelength is approximately linearly proportional to the pump power as shown in Fig. 4-15. The lasing wavelength increases about 2.6 nm when the average pump power is varied from 8μW to 68μW. The increasing rate is about 0.043 nm/μW.

In order to further characterize and analyze the thermal effects, we design a thermo-electric cooler (TEC) system and put the sample on a copper which is mounted on the TEC system to stabilize the substrate temperature at room temperature or vary the substrate temperature from room temperature to as high as 47°C. The configuration of the TEC system is shown in Fig. 4-16. In this TEC system, a 10 kΩ thermistor with ±0.01°C accuracy is used to monitor the temperature of the sample. The thermistor feedbacks data to the temperature controller, Newport-325B, in order to decide the driving current of the TEC. A stable

temperature is achieved in 10 seconds. We mount our sample on the copper in order to control its substrate temperature.

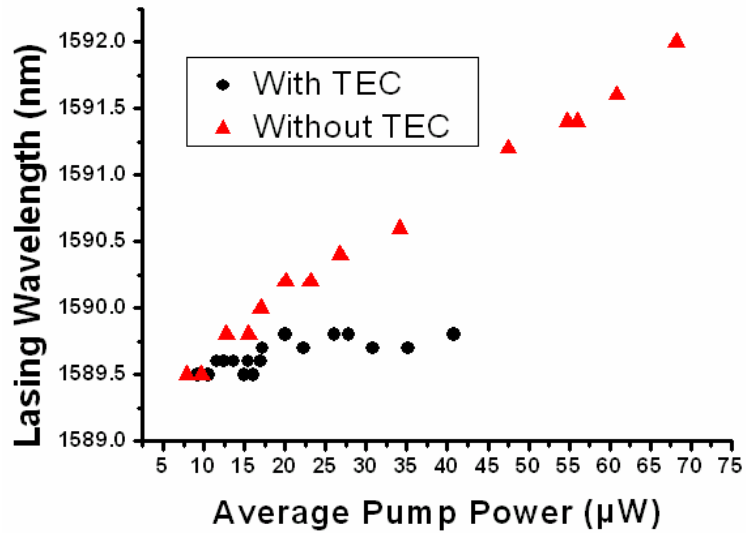Fig. 4-15.   The red shift of lasing wavelength is about 2.6 nm when the average pump power increases 60 µW. The variation of lasing wavelength is improved to within 0.3 nm when the TEC system is used.
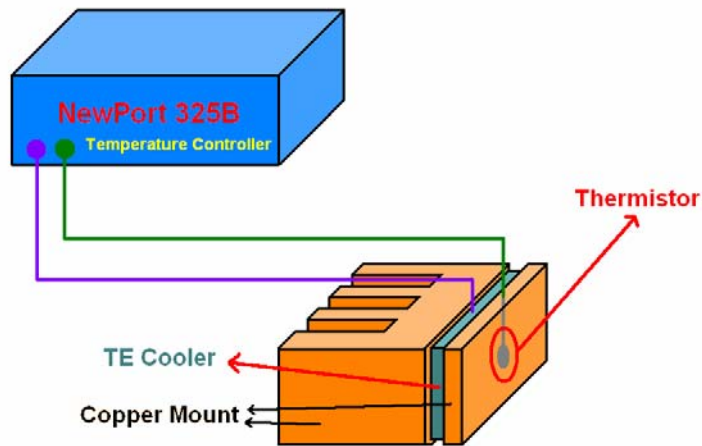

Fig. 4-16.   The configuration of our TEC system.

We observe a significant improvement of the red shift effect when TEC system is used to fix the substrate temperature at 25°C as shown in Fig. 4-15. The variation of lasing

wavelength due to increasing pump power can be controlled to within 0.3 nm. This number can be further reduced by improving the contact between the copper and the sample in our setup.

Threshold dependence on substrate temperatures of the two-dimensional photonic crystal lasers is investigated. The substrate temperature is stabilized at different values by using the TEC system. The threshold average pump powers for different substrate temperatures are listed in Table 4-2 with 1.5% duty cycle at 0.5 MHz repetition rate. It is obvious that the threshold of the laser cavity increases with the substrate temperature. This agrees well with the results reported in reference [22].

Table 4-2.   The threshold pump powers with different substrate temperatures.

Substrate Temperature (°C)	Threshold Power (µW)
24	6.8
30	10.3
36	14.8
42	20.2

The red shift rate of lasing wavelength with increasing substrate temperature is 0.067nm/K as shown in Fig. 4-17. This property can be used to tune the lasing wavelength of two-dimensional photonic crystal lasers without changing the pattern design. The red shift of lasing wavelength with increasing pump power or/and substrate temperature is caused by the changes of material index and cavity volume due to increasing of the cavity temperature [22, 23]. This can be illustrated by the following equation:

$$\frac{d\lambda / dT}{\lambda} = \frac{dL / dT}{L} + \frac{dn / dT}{n} \tag{3}$$

where λ, n, T, and L denote lasing wavelength, refractive index, cavity temperature, and effective cavity length of resonance mode, respectively. The terms *dL/L* and *dn/n* are about

5×10^{-6} and 2×10^{-4}. As a result, the variation of refractive index dominates the red shift of lasing wavelength and the thermal expansion of cavity volume can be neglected.
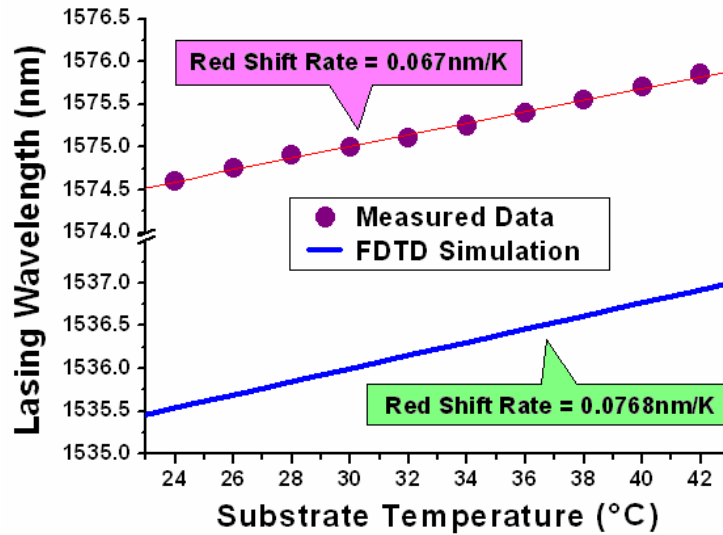
Fig. 4-17.   The measured lasing wavelengths with increasing substrate temperature are represented by circles and its increasing rate is 0.067 nm/K by using a linear fit. The lower solid line is the simulated red shift curve using the FDTD method. Its increasing rate is 0.0768 nm/K.

The change of index of refraction of InP with temperature *dn / dT* is about 2×10^{-4} /°C. According to this number, the calculated red shift curve of lasing wavelength with increasing substrate temperature obtained by using the FDTD method is also shown in Fig. 4-17. The simulated red shift rate is 0.077nm/K, which matches with the measurement results quite well. The small difference between these two results can be attributed to the imperfect contact in our TEC system that we mentioned before and the effects caused by the small variation of the cavity volume we neglect in our simulation. In addition, there is a 40 nm difference between the simulated and measured lasing wavelengths. This is caused by the high temperature of micro-cavity region under optical pumping and the uncertainty of r/a ratio of our devices.

We also investigate threshold dependence on different pumping conditions. We turn off the TEC system and change the condition of our pumping source for three different duty cycles, 1%, 1.5%, and 2%. With these three conditions, we obtain three corresponding L-L curves shown in Fig. 4-18. An ultra-low threshold average pump power about 3.4 μW is obtained with 1% duty cycle pumping condition. The threshold average pump powers for 1.5% and 2% duty cycles are 4.3 μW and 6.1 μW, respectively. The increasing duty cycle causes cavity temperature to rise and hence leads to the reduction of gain peak of the QWs. When the gain decreases, threshold increases. In addition, the variation of duty cycles would also affect the alignment between the gain peak of QWs and the lasing mode and hence influence the threshold pump power.
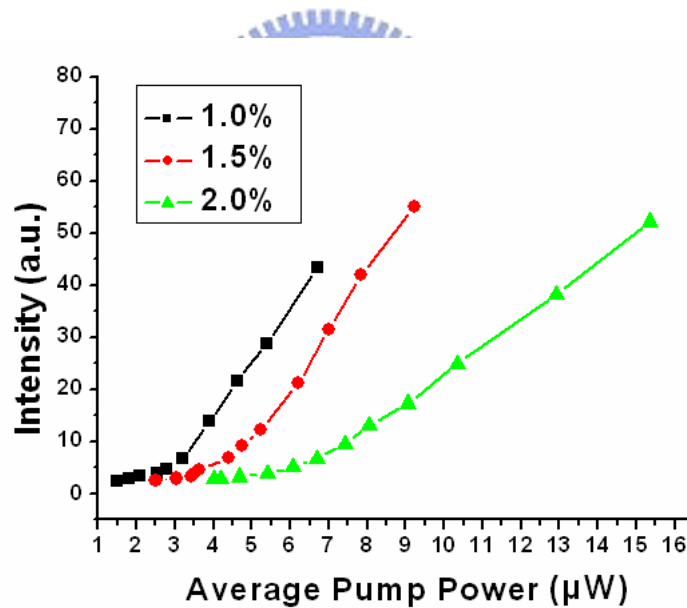

Fig. 4-18.   There is strong dependence of threshold pump power on the duty cycle of the pump source. The threshold pump powers for 1%, 1.5%, and 2% duty cycles are 3.4 μW, 4.3 μW, and 6.1 μW, respectively.

According to the results obtained by varying substrate temperatures, we can estimate the temperature raise and red shift of lasing wavelength due to increasing of duty cycle, and they

are about 4 K/(1% duty cycle) and 0.27 nm/(1% duty cycle). Actually the measured red shift

of lasing wavelength caused by increasing duty cycle is 0.34 nm/(1% duty cycle). We can also

estimate the red shift of lasing wavelength with respect to substrate temperature caused by

increasing duty cycle, which is about 0.085 nm/K, and the actual measured value is 0.067

nm/K. This difference is still in the range of our measurement tolerance and the two values

approximately match with each other. In fact, the variation caused by thermal effects is

usually expressed exponentially, but this exponential behavior is not so obvious within the

range we measured. As a result, a linear approximation is used in the above calculations.

The lasing wavelength and threshold pump power both depend on the thermal effects

caused by different pumping conditions and substrate temperatures. These thermal effects are

significant due to poor heat dissipation of air in the membrane structure. Actually, we can

calculate the thermal resistance of these two-dimensional photonic crystal lasers to show how

serious the thermal effects are. The thermal resistance R_{th} is generally defined as:

$$R_{th} \equiv \frac{\Delta T}{\Delta P_{th}} = \frac{\Delta \lambda}{\Delta P_{th}} / \frac{\Delta \lambda}{\Delta T} \qquad (4)$$

The thermal power P_{th} is defined as the difference between the pump power absorbed by the

cavity P_{ab} and the optical output power P_{out}, i.e. $P_{th}=P_{ab}-P_{out}$. In fact, most absorbed pump

power is dissipated in terms of heat and is much higher than the optical output power. As a

result, we assume that $P_{ab}>>P_{out}$, i.e. $P_{th} \sim P_{ab}$, which can be estimated to be about 30% of

the input pump power. $\Delta\lambda/\Delta P_{th}$ and $\Delta\lambda/\Delta T$ denote the lasing wavelength variation caused by

different absorbed pump powers and substrate temperatures, respectively. We can obtain these

data from our measurement results. The calculated thermal resistance R_{th} is then about 2×10^3

K/mW. The typical R_{th} value of general VCSELs with 5μm × 5μm oxidation aperture is

about 2 K/mW [24]. Our micro-cavity area is about 10 μm^2, which is a little smaller than the

oxidation aperture of general VCSELs. However, its thermal resistance is about 1000 times

higher than that of VCSELs.

In my opinion, the above temperature-dependent properties of two-dimensional photonic crystal lasers may be useful in real applications such as thermal-tuning light sources in the WDM systems and thermal sensor applications. However, all of these thermal effects we investigate have to be improved for continuous-wave-operation proposition, and this can be achieved by using a low-index substrate such as sapphire with higher thermal conductivity as the heat sink. We think this could significantly reduce the thermal effects and continuous-wave operation can be realized.

4-5. Conclusion

In the first section of this chapter, we setup a NIR micro-PL system with nano-scale spectrum resolution to measure the devices. In the second section, the basic characteristics including the L-L curve, lasing spectrum, and the resonance modes of D3 micro-cavity are measured and discussed.

In the third section, we show the tuning properties of lasing wavelength by varying the r/a ratio and lattice constant of photonic crystal patterns. This would be a potential light source for WDM systems.

In the forth section, we measure and analyze the thermal effects of two-dimensional photonic crystal membrane lasers. We setup a TEC system in our experiment. The thermal tuning property of lasing wavelength caused by different substrate temperatures is investigated both in experiment and simulation. The threshold dependence on thermal effects caused by different substrate temperatures and pump conditions are also investigated. An ultra low threshold 3.4 W is obtained under 1% pump duty cycle. At last, we calculate its thermal resistance and compare it with that of VCSELs.

5. Conclusion

In this thesis, we calculate the band diagrams, band-gaps, resonance spectrum, and lasing mode profile of the symmetric and asymmetric two-dimensional photonic crystal lasers using 3D plane-wave-expansion (PWE) method and finite-difference time-domain (FDTD) method. These help us to optimize our photonic crystal design. According to these, we make good alignments between the resonance modes and gain spectrum of MQWs. Further modification of the photonic crystal micro-cavity will be designed for future work.

We also present the fabrication processes of two different structures. In the symmetric structure case, a two-dimensional photonic crystal membrane is fabricated. In the asymmetric structure case, the wafer-bonding technology is developed. And we also propose a brand new and efficient fabrication method of asymmetric structure by using glue-bonding technology and focused-ion-beam (FIB) system.
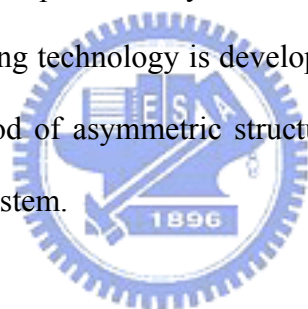
In order to characterize the photonic crystal lasers, a micro-photo-luminescence (PL) system is setup. The micro-scale and nano-scale resolutions in microscopic system and spectrum analysis have been achieved. An excellent sensitivity of this system is presented in this thesis. By using this system, the basic characteristics of two-dimensional photonic crystal cavities are measured. Over ten resonance modes are observed in a D3 cavity.

At last, we setup a thermo-electro cooler (TEC) system in order to characterize the thermal properties of two-dimensional photonic crystal lasers at different substrate temperatures with different pump conditions. The red shift of lasing wavelength with different substrate temperatures is measured and calculated. We also investigate the threshold dependence on different substrate temperatures and pump conditions. We also calculate the

thermal resistance of D3 photonic crystal micro-cavity and compare it with that of the general VCSELs. The much larger thermal resistance of the photonic crystal membrane lasers can be improved by employing a sapphire substrate.

References

[1]   E. Yablonovitch, *Phys. Rev. Lett.* **vol. 58**, pp. 2059-2062, 1987

[2]   J. D. Joannopoulos, R. D. Meade, J. N. Winn, *Princeton University Press*, 1995

[3]   Y.-H. Lee, H.-Y. Ryu, *IEEE Circuit & Devices Magazine,* pp. 8-15, 2002

[4]   E. M. Purcell, *Phys. Rev.* **vol. 69**, p. 681, 1946

[5]   O. Painter, R.-K. Lee, A. Scherer, A. Yariv, J. D. O'Brien, P. D. Dapkus, and I. Kim, *Science* **vol. 284**, pp. 1819-1821, 1999

[6] O. Painter, J. Vuckovic, and A. Scherer, *J. Opt. Soc. Amer. B* **vol. 16**, pp. 275-285, 1999

[7] H.-Y. Ryu, H.-G. Park, and Y.-H. Lee, *IEEE J. Select. Topics Quantum Electron.* **vol. 4**, pp. 891-908, 2002

[8] H.-Y. Ryu, S.-H. kim, H.-G. Park, J.-K. Hwang, Y.-H. Lee, and J.-S. Kim, *Appl. Phys. Lett.* **vol. 80**, pp. 3883-3885, 2002

[9]   K. hennessy, C. Reese, A. Badolato, C.-F. Wang, A. Imamoglu, G. Jin, S. Shi, and D.-W. Prather, *Appl. Phys. Lett.* **vol. 83**, pp. 3650-3652, 2003

[10] H.-Y. Ryu, J.-K. Hwang, and Y.-H. Lee, *IEEE J. Quantum Electron.* **vol. 39**, pp. 314-322, 2003

[11] P. R. Berman, *New York: Academic*, 1994

[12] H.-G. Park, J.-K. Hwang, J. Hoon, H.-Y. Ryu, S.-H. Kim, J.-S. Kim, Y.-H. Lee, *IEEE J. Quantum Electron.* **vol. 38**, pp. 1353-1365, 2002

[13] H.-Y. Ryu, M. Notomi, and Y.-H. Lee, *Appl. Phys. Lett.* **vol. 83**, pp. 4294-4296, 2003

[14] M. Loncar, M. Hochberg, A. Scherer, and Y. Qiu, *Opt. Lett.* **vol. 29**, pp. 721-723, 2004

[15] J.-R. Cao, W. Kuang, Z.-J. Wei, S.-J. Choi, H. Yu, M. Bagheri, J. D. O'Brien, P. D. Dapkus, *IEEE Photon. Technol. Lett.* 2005

[16] J.-K. Hwang, H.-Y. Ryu, D.-S. Song, I.-Y. Han, H.-K. Park, D.-H. Jang, and Y.-H. Lee, *IEEE Photon. Technol. Lett.* **vol. 12**, pp. 1295-1297, 2000

[17] H.-G. Park, S.-H. Kim, S.-H. Kwon, Y.-G. Ju, J.-K. Yang, J.-H. Baek, S.-B. Kim, and Y.-H. Lee, *Science* **vol. 305**, pp. 1444-1447, 2004

[18] C.-W. Kim, W.-J. Kim, A. Stapleton, J.-R. Cao, J. D. O'Brien, and P. D. Dapkus, *J. Opt. Soc. Amer. B* **vol. 19**, pp. 1777-1781, 2002

[19] L. A. Coldren, K. Furuya, and B. I. Miller, *J. electrochem. Soc.* **vol. 31**, p. 1918, 1983

[20] W.-Kuang, J.-R. Cao, S.-J. Choi, J. D. O'Brien, P. D. Dapkus. *IEEE Photon. Technol. Lett.* **vol. 17**, pp. 941-943, 2005

[21] J.-R. Cao, W. Kuang, S.-J. Choi, P.-T. Lee, J. D. O'Brien, *Appl. Phys. Lett.* **vol. 83**, pp. 4107-4109, 2003

[22] P.-T. Lee, J.-R. Cao, S.-J. Choi, Z.-J. Wei, J. D. O'Brien, *Appl. Phys. Lett.* **vol. 81**, pp. 3311-3313, 2002

[23] B. Wild, R. Ferrini, R. Houdre, M. Mulot, S. Anand, and C. J. M. Smith, *Appl. Phys. Lett.* **vol. 84**, pp. 846-848, 2004

[24] J. Talghader, and J. S. Smith, *Appl. Phys. Lett.* **vol. 66**, pp. 335-337, 1995